

國立交通大學

光電工程研究所

碩士論文

極化式編碼於孔徑函數上之應用

Polarization Coded Aperture Engineering

研究生：鍾議寬

指導教授：田仲豪 副教授

中華民國一百年七月

極化式編碼於孔徑函數上之應用

Polarization Coded Aperture Engineering

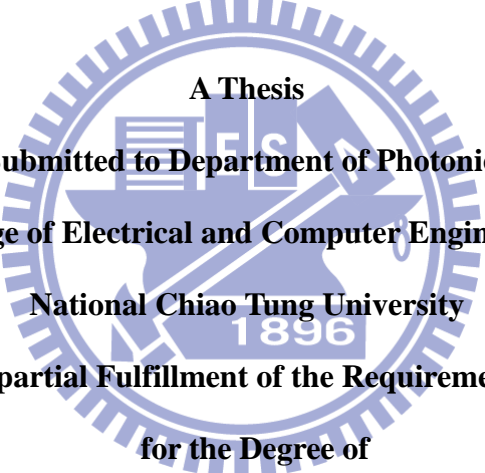
研究生：鍾議寬

Student: Yi-Kuan Chung

指導教授：田仲豪

Advisor: Chung-Hao Tien

國立交通大學
光電工程研究所
碩士論文

The logo of National Chiao Tung University is a circular emblem with a gear-like outer border. Inside the circle, there is a stylized representation of a building or a bridge structure. The letters 'NCTU' are prominently displayed in the center, with the year '1896' below it. The text 'National Chiao Tung University' is written around the inner perimeter of the circle.

A Thesis
Submitted to Department of Photonics
College of Electrical and Computer Engineering
National Chiao Tung University
in partial Fulfillment of the Requirements
for the Degree of
Master
in
Department of Photonics
July 2010

Hsinchu, Taiwan, Republic of China

中華民國一百年七月

極化式編碼於 孔徑函數上之應用

碩士研究生：鍾議寬 指導教授：田仲豪

國立交通大學
光電工程研究所

摘要

繞射理論可依據觀測材料的特性與觀測維度的大小，分成將電磁場視為純量的純量繞射理論與實際考量各點邊界條件解出該點電磁場，計算上較為複雜的向量繞射。以往，於空間解析度低的情況下(低數值孔徑)，採用純量繞射已可得到不錯的近似解；然而，由於科技的日益進步，空間解析度也日漸增加(高數值孔徑)，光的向量特性必須加以考量，此時純量繞射已不再適用，必須採用向量繞射來解釋。

因此，於此篇論文中，首先會針對各種極化於聚焦平面上的場形分布做討論，指出不同極化於高數值孔徑的系統下，聚焦場形之各種特性。接著，考量到極化於日後顯微系統的影響，我們利用不同或高階數的非勻質極化於孔徑上的分布，來達到拓展景深的應用；之後再藉由創造出的多波長非勻質極化光，將其應用至表面電漿領域，建立一個即時之感測系統，並提出一金屬-絕緣層-金屬的結構，來完善此感測系統。

Polarization Coded Aperture Engineering

Master student: Yi-Kuan Chung

Advisor: Dr. Chung-Hao Tien

Institute of Electro-Optical Engineering

National Chiao Tung University

Abstract

In the diffraction theory, scalar diffraction theory is based on specific material condition or observed with low NA system, the fields are treated as the scalar components to obtain a good approximation by relatively simple mathematics formula. However, while the technique was fast developed, the dimension and materials is more and more small and variety, respectively. Therefore, the vectorial properties of light are no longer neglected in the discussion of polarization.

In this thesis, first part was addressed about the effect of polarization in different numerical apertures, the influence of polarization is more distinct as numerical aperture increases. The second part was addressed to discuss extending depth of focus by the synthesis of polarizations. The third part is to build up a polychromatic SPR sensor system utilized excited chromatic radially polarized light and optimize the system by purposed metal-insulator-metal (MIM) structure.

誌謝

首先感謝指導教授 田仲豪老師兩年來在研究上給予的指導、並時常分享學習上以及人生經歷上的寶貴經驗，讓我除了能夠順利完成學業及此論文外，也了解到很多待人處事上該有的態度。

還必須感謝的是實驗室中帶領我一步一步學習到畢業的子翔學長，還有給予許多關於學習相關經驗的小陸學長、健翔學長、進哥學長、壯哥學長。以及一起努力到畢業的同伴鍾岳，在研究的路途上，因為有你們的陪伴使我能夠更順利地走完這趟學習之路。同時感謝實驗室的杰恩學弟、國恩學弟、孟潔學妹，希望明年你們也能順利畢業。額外感謝益智學長在玩樂時間的陪伴。

再來感謝我的家人，從小栽培我到大，能夠讓我無後顧之憂地完成學業，並永遠支持著我，也感謝我的女朋友，能夠體諒我因為研究而無法時常陪伴在她身邊，並分擔著我的煩惱與憂愁，最後也感謝其他的朋友們，因為你們，讓我在學習的路上並不孤單，在此，將畢業的喜悅分享給大家。

Table of Contents

Abstract(Chinese)	i
Abstract(English)	ii
Acknowledgement	iii
Table of Contents	iv
Figure Captions	v
List of tables	viii
Chapter 1 <i>Introduction</i>	1
1.1 Scalar diffraction theory.....	1
1.1.1 Kirchhoff diffraction formula.....	2
1.1.2 Fresnel-Kirchhoff diffraction formula.....	4
1.1.3 Rayleigh-Sommerfeld diffraction formula.....	5
1.2 Vector diffraction theory.....	7
1.2.1 Vectorial Debye theory.....	7
1.2.2 Fresnel's equations.....	7
1.2.3 Jones calculus.....	9
1.3 Comparison of two diffraction theory.....	11
1.4 Motivation & Organization.....	11
Chapter 2 <i>Polarization Beams</i>	16
2.1 Homogeneous and inhomogeneous polarization.....	16
2.2 Properties of polarized beam.....	17
2.2.1 Linear polarization.....	17
2.2.2 Circular polarization.....	19
2.2.3 Radial polarization.....	20
2.2.4 Azimuthal polarization.....	21
2.3 Summary.....	21
Chapter 3 <i>Application 1 – Extended Depth of Focus</i>	23
3.1 History and Principle.....	23
3.2 Combination of inhomogeneous beams.....	27
3.3 Higher-order radially polarized beam.....	32
3.4 Summary.....	33

Chapter 4 Application 2 – Chromatic Surface Plasmon Resonance...	35
4.1 History and Principle	35
4.2 Experimental Setup.....	39
4.2.1 Synthesis of radially polarized white light.....	41
4.2.2 MIM Structure.....	42
4.3 Matrix method.....	44
4.4 Simulation and Experimental Data.....	46
4.5 Summary.....	51
Chapter 5 Conclusions and Future work.....	52
5.1 Conclusions.....	52
5.2 Future work.....	53
Reference.....	54

Figure Captions

Fig. 1-1 Slice through the volume V	3
Fig. 1-2 A plane screen with point-source illumination.....	4
Fig. 1-3 Green's function in a diffraction plane by means of the mirror method.	6
Fig. 1-4 The schematic diagram of a_ρ , a_φ , \hat{x} and \hat{y}	8
Fig. 1-5 A side view of the generalized optical system.	9
Fig. 1-6 Geometry of Fresnel's equations for (a) s-polarization and (b) p-polarization.	10
Fig. 2-1 (a) and (b) illustrates the homogeneous and in homogeneous beam, respectively.	16
Fig. 2-2 Intensity distribution of the cylindrical vector beams. (a) Radial (b) Azimuthal polarization.	17
Fig. 2-3 Intensity profile of linearly polarized focus as numerical aperture increases from 0.2 to 1.0, where the vectorial feature becomes more apparent with high-NA system.	18

Fig. 2-4 Intensity profile of circular polarized focus for increasing numerical aperture.	19
Fig. 2-5 Intensity profile of radially polarized beams in different numerical aperture. When numerical aperture increased, the optical field is transformed from a doughnut-shaped to a flat-topped shape.	21
Fig. 2-6 Focused intensity profile of azimuthally polarized beams for high numerical aperture.	21
Fig. 2-7 Each component of focal fields in azimuthally polarized light, due to the destructive interference of depolarization effect, the electric field of z-component is zero.	22
Fig. 3-1 The configuration for annular aperture.	25
Fig. 3-2 The schematically concept of extending depth of focus by refractive optics.	26
Fig. 3-3 The polarization coded aperture.	27
Fig. 3-4 Two types of radial and azimuthal combination.	28
Fig. 3-5 (a) to (j) peak intensity across different z-axis position when radially polarized light is in outer ring region.	29
Fig. 3-6 (a) to (j) peak intensity across different z-axis position when azimuthally polarized light is in outer ring region.	30
Fig. 3-7 The FWHM of (a) radially polarized light and (b) azimuthally polarized light focal fields.	31
Fig. 3-8 The intensity profile comparison between linear polarization coded aperture and in homogeneous coded aperture on x-y dimension.	31
Fig. 3-9 The fundamental mode (R-TEM ₀₁) and two higher-order modes (R-TEM ₁₁ and R-TEM ₂₁) of radially polarized beam.	32
Fig. 3-10 The FWHM of focal fields of different order of radially polarized beam.	33

Fig. 4-1 (a) s-polarization (b) p-polarization waves propagate between two media. ..36	36
Fig. 4-2 configuration of the PC-RPSPR sensor, where CL: collimated lens, SVP: spatial varying polarizer, RL: relay lens, BS: beam splitter, IL: image lens, MIM: metal-insulator-metal structure. The insets show (a) the photo of SVP, (b) the schematic diagram of MIM structure.40	40
Fig. 4-3 The SVP assembly, which is composed of eight sectors.41	41
Fig. 4-4 Comparison with the different test sample. (a) and (c) are experimental data and (b) and (d) are simulation when test sample is air and water, respectively.(e) and (f) are the slice of (b) and (d), respectively. The wavelength here is 610 nm.43	43
Fig. 4-5 Obviously angular shift in T-SPR modes by comparing the different refractive index of test sample.44	44
Fig. 4-6 Geometry for propagation matrix.45	45
Fig. 4-7 Schematic drawing showing the matrix method.46	46
Fig. 4-8 Radially polarized white light generated by radial polarizer. The arrows indicate the axis direction of analyzer.47	47
Fig. 4-9 The (a) experimental and (b) simulated observation of reflected rainbow disk for the case of free space in contact with the gold monolayer structure, where subfigures 1 to 3 are respectively show the dark resonance ring observed at wavelength $\lambda = 610$ nm, 530 nm, and 450 nm.48	48
Fig. 4-10 comparison shows the effect of MIM structure ($\lambda=610$ nm).49	49
Fig. 4-11 (a) rainbow concentric ring in different sensing condition (b) the spectra distribution of rainbow concentric rings as the medium above the MIM structure is chosen saline with different concentration.50	50
Fig. 5-1 the productive procedure of data cube in white light RP-SPR.53	53

List of Table

Table 1-1 The reference between polarization and Jones vector.12

Table 1-2 The reference between optical elements and Jones matrices.13



Chapter 1

Introduction

Diffraction denotes the deviation of light rays from rectilinear propagation which cannot be interpreted by either refraction or reflection. The diffraction theory can be divided into two parts which is based on solving the boundary condition problem or not. In this chapter, we will introduce two diffraction theories, then compare to each other.

1.1 Scalar diffraction theory

Classical scalar diffraction theory does not solve the boundary condition problem but a boundary value problem; it means that scalar diffraction theory is able to describe diffraction of light via a simple mathematical formula, because the hypotheses of material lead to all components of the electric and magnetic field having identical behavior which is fully described by a single scalar wave equation [1].

If the propagation medium is linear, isotropic, homogeneous, non-dispersive, nonmagnetic, then applying the $\nabla \times$ operation to the Maxwell equation

$$\nabla \times (\nabla \times \vec{H}) = \varepsilon \frac{d(\nabla \times \vec{E})}{dt} \quad (1.1a)$$

$$\nabla \times (\nabla \times \vec{E}) = -u \frac{d(\nabla \times \vec{H})}{dt} \quad (1.1b)$$

$$\nabla \times (\nabla \times \vec{u}) = \nabla(\nabla \cdot \vec{u}) - \nabla^2 \vec{u} \quad (1.1c)$$

Where u represents any of the vector field components, substitution of the Eq. (1.1a) and Eq. (1.1b) in Eq. (1.1c) yields

$$\nabla^2 \vec{H} - \frac{n^2}{c^2} \frac{\partial^2 \vec{H}}{\partial t^2} = 0 \quad (1.2a)$$

$$\nabla^2 \vec{E} - \frac{n^2}{c^2} \frac{\partial^2 \vec{E}}{\partial t^2} = 0 \quad (1.2b)$$

Where n is the refractive index of the medium, defined by

$$n = \left(\frac{\varepsilon}{\varepsilon_0} \right)^{1/2} \quad (1.3a)$$

And c is the velocity of propagation in vacuum, written as

$$c = \frac{1}{\sqrt{\mu_0 \varepsilon_0}} \quad (1.3b)$$

Since the Eq. (1.2a) and Eq. (1.2b) can apply for both electric and magnetic field, therefore, it is possible to summarize the behavior of all components of electric and magnetic field through a single scalar wave equation

$$\nabla^2 u(P, t) - \frac{n^2}{c^2} \frac{\partial^2 u(P, t)}{\partial t^2} = 0 \quad (1.4)$$

Where $u(P, t)$ represents any scalar field components of electric and magnetic field, and the components dependent on both position P in space and time t .

From above we assume that propagation medium is linear, isotropic, homogeneous, non-dispersive, nonmagnetic, then we can treat the electric and magnetic field as a scalar field to simplify the behavior of diffraction. The scalar diffraction theory is well known as Fourier optics.

1.1.1 Kirchhoff diffraction formula

The Kirchhoff diffraction formula is a solution of the scalar, time-independent wave equation using Green's relation

$$\begin{aligned} & \iiint_V (U(P) \nabla^2 G(P) - G(P) \nabla^2 U(P)) dv \\ &= \oiint_{S=S_1+S_2} \left(U(P) \frac{\partial G(P)}{\partial n} - G(P) \frac{\partial U(P)}{\partial n} \right) ds \quad (1.5) \end{aligned}$$

Where V is an arbitrary closed volume with closed surface S , n is the outward normal

direction at each point on S . $U(P)$ and $G(P)$ are any function of position. As shown in

Fig. 1-1

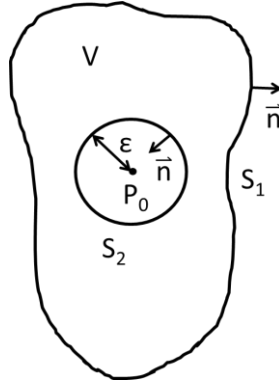


Fig 1-1 Slice through the volume V .

If U and G both satisfy the free-space Helmholtz equation.

$$(\nabla^2 + k^2)G = 0 \quad (1.6a)$$

$$(\nabla^2 + k^2)U = 0 \quad (1.6b)$$

Substituting the Eq. (1.6a) and Eq. (1.6b) in the Eq. (1.5), we obtain

$$\iint_{S=S_1+S_2} \left(U \frac{\partial G}{\partial n} - G \frac{\partial U}{\partial n} \right) ds = 0 \quad (1.7)$$

Choosing a spherical wave as an auxiliary function expanding at the point P_0 , then the value of G at arbitrary point P_1 is given by

$$G(P_1) = \frac{\exp(ikr_{01})}{r_{01}}$$

And

$$\frac{\partial G(P_1)}{\partial n} = \cos(\vec{n}, \vec{r}_{01}) \left(ik - \frac{1}{r_{01}} \right) \frac{\exp(ikr_{01})}{r_{01}} \quad (1.8)$$

Where r_{01} is the length of vector \vec{r}_{01} pointing from P_0 to P_1 . For a particular case of P_1 on S_2 , $\cos(\vec{n}, \vec{r}_{01}) = -1$, the Eq. (1.8) become

$$G(P_1) = \frac{e^{ik\epsilon}}{\epsilon} \quad \text{and} \quad \frac{\partial G(P_1)}{\partial n} = \left(\frac{1}{\epsilon} - ik \right) \frac{e^{ik\epsilon}}{\epsilon} \quad (1.9)$$

Letting ϵ is tending to zero, then

$$\begin{aligned}
& \lim_{\varepsilon \rightarrow 0} \iint_{S_2} \left(U \frac{\partial G}{\partial n} - G \frac{\partial U}{\partial n} \right) ds \\
&= \lim_{\varepsilon \rightarrow 0} 4\pi\varepsilon^2 \left[U(P_0) \left(\frac{1}{\varepsilon} - ik \right) \frac{e^{ik\varepsilon}}{\varepsilon} - \frac{\partial U(P_0)}{\partial n} \frac{e^{ik\varepsilon}}{\varepsilon} \right] = 4\pi U(P_0)
\end{aligned} \tag{1.10}$$

Substitution of this result in Eq. (1.7) yields

$$U(P_0) = \frac{1}{4\pi} \iint_{S_1} \left\{ \frac{\partial U}{\partial n} \left[\frac{\exp(ikr_{01})}{r_{01}} \right] - U \frac{\partial}{\partial n} \left[\frac{\exp(ikr_{01})}{r_{01}} \right] \right\} ds \tag{1.11}$$

This result allows the field at any point P_0 to be expressed in terms of the “boundary values” of the spherical wave on any closed surface, it is known as the Kirchhoff diffraction formula.

1.1.2 Fresnel-Kirchhoff diffraction formula

Furthermore, considering the distance r_{01} from the aperture A to the observation point is many times of optical wavelength, so we have $k \gg 1/r_{01}$, and Eq. (1.8) become

$$\begin{aligned}
\frac{\partial G(P_1)}{\partial n} &= \cos(\vec{n}, \vec{r}_{01}) \left(ik - \frac{1}{r_{01}} \right) \frac{\exp(ikr_{01})}{r_{01}} \\
&\approx ik \cos(\vec{n}, \vec{r}_{01}) \frac{\exp(ikr_{01})}{r_{01}}
\end{aligned} \tag{1.12}$$

Substitution of this result in Eq. (1.11), we find

$$U(P_0) = \frac{1}{4\pi} \iint_A \frac{\exp(ikr_{01})}{r_{01}} \left[\frac{\partial U}{\partial n} - ikU \cos(\vec{n}, \vec{r}_{01}) \right] ds \tag{1.13}$$

Now supposing there is a single spherical wave which illuminates the aperture from P_2 to P_1 , as shown in Fig. 1-2.

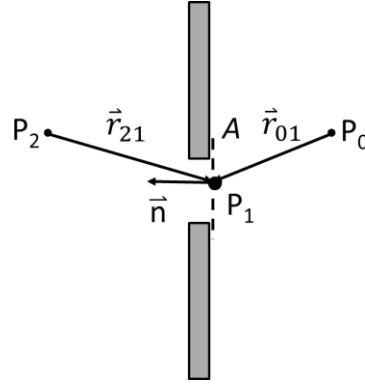


Fig. 1-2 A plane screen with point-source illumination.

$$U(P_1) = \frac{A \exp(ikr_{21})}{r_{21}} \quad (1.14)$$

If r_{21} is similar to r_{01} which is many times of optical wavelength, Eq. (1.13) can be reduced

$$U(P_0) = \frac{A}{i\lambda} \iint_{\phi} \frac{\exp[ik(r_{01} + r_{21})]}{r_{01}r_{21}} \left[\frac{\cos(\vec{n}, \vec{r}_{01}) - \cos(\vec{n}, \vec{r}_{21})}{2} \right] ds \quad (1.15)$$

This result only holds for illumination of a single point source, known as the Fresnel-Kirchhoff diffraction formula. So far, above derivation is restricted to an aperture illumination consisting of a single spherical wave, such restriction will be moved by the Rayleigh-Sommerfeld theory.

1.1.3 Rayleigh-Sommerfeld diffraction formula

Although the Fresnel-Kirchhoff theory has been widely used in practice, it still has inconsistent due to the theory showing failure when assumed boundary conditions as the observation point approaches the screen or aperture. Therefore, Sommerfeld corrected the theory.

If U is a boundary value on the screen, G must be zero there so that the second term in vanishes, similarly, if $\partial U / \partial n$ is the boundary value, $\partial G / \partial n$ must be zero in order for the first term to vanish. For both conditions, G must satisfies the Helmholtz

equation and Sommerfeld's radiation condition (Eq. 1.16)

$$\lim_{R \rightarrow \infty} R \left(\frac{\partial U}{\partial n} - ikU \right) = 0 \quad (1.16)$$

Consider a particular case for a plane screen, as shown in Fig. 1-3. Green's function is determined by mirror method and formed from the superposition of two spherical waves.

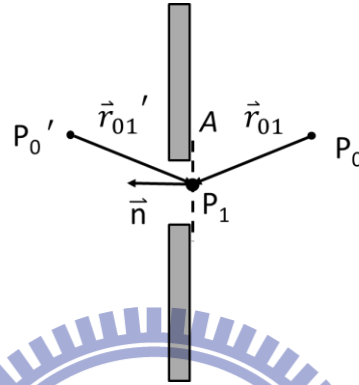


Fig. 1-3 Green's function in a diffraction plane by means of the mirror method.

If U is the boundary value, that is the First Rayleigh-Sommerfeld solution. It can be expressed as

$$U_I(P_0) = \frac{-1}{2\pi} \iint_A U \frac{\partial G}{\partial n} ds \quad (1.17)$$

If $\frac{\partial U}{\partial n}$ is the boundary value, that is the Second Rayleigh-Sommerfeld solution. It can be expressed as

$$U_{II}(P_0) = \frac{1}{2\pi} \iint_A \frac{\partial U}{\partial n} G ds \quad (1.18)$$

Then substituted Eq. (1.12) and Eq. (1.14) into Eq. (1.17), we can find

$$U_I(P_0) = \frac{A}{i\lambda} \iint_A \frac{\exp[ik(r_{01} + r_{21})]}{r_{01}r_{21}} \cos(\vec{n}, \vec{r}_{01}) ds \quad (1.19)$$

This result is known as the Rayleigh-Sommerfeld diffraction formula, and it includes the significance of Huygens-Fresnel principle, we can rewrite the mathematically as

$$U(P_0) = \frac{1}{i\lambda} \iint_A U(P_1) \frac{\exp(ikr_{01})}{r_{01}} \cos \theta \, ds \quad (1.20)$$

It expresses the observed field $U(P_0)$ as a superposition of diverging spherical waves $\frac{\exp(ikr_{01})}{r_{01}}$ originating from secondary sources located at each and every point P_1 within the aperture A . So far, through the endeavor of Kirchhoff and Sommerfeld, the scalar diffraction theory developed steady. Afterward, the theory became more complete by Fresnel and Fraunhofer.

1.2 Vector diffraction theory

From above, we can know that scalar diffraction theory is based on certain hypotheses of material, and did not consider the boundary condition problem. Therefore, scalar diffraction theory has a simple way to obtain analytical solution. In vector diffraction theory, the any kind of materials and boundary condition problem will be considered; it means that every analytical solution must goes through many times complex calculation due to the vector electric fields component of every direction will be calculated by Maxwell's equation and boundary condition [2].

1.2.1 Vectorial Debye theory

When vectorial properties of electromagnetic fields are considered, the fields cannot be treat as scalar, it means that the different component of electric fields will couple into each other, the phenomenon is so-called depolarization. Especially in the higher numerical aperture objective system, depolarization effect is more obvious.

In order to confirm this effect, we assume a linear polarized incident light which along the x-axis. For the polar coordinate

$$E_i(r) = P(r)\cos\varphi a_\rho - P(r)\sin\varphi a_\varphi \quad (1.21)$$

The $P(r)$ is the amplitude distribution within the lens aperture, a_ρ and a_φ is the unit vectors in ρ and φ directions. As depicted in Fig 1-4. Then utilized the vectorial Debye integral

$$E(P_2) = \frac{i}{\lambda} \iint_{\Omega} E_0(P_1) \exp(-is \cdot R) d\Omega \quad (1.22)$$

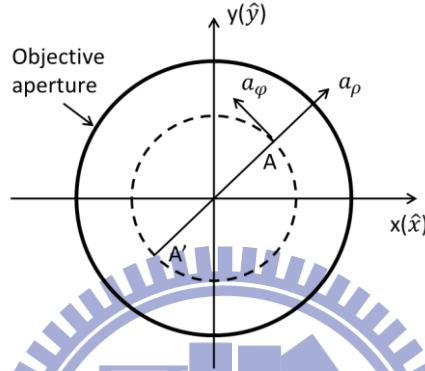


Fig. 1-4 The schematic diagram of a_ρ , a_φ , \hat{x} and \hat{y} .

The $E(P_2)$ is an electric fields at point P_2 in the focal region of an objective and the $E_0(P_1)$ at point P_1 on the reference sphere surface. Therefore the P_1 and P_2 are represented by spherical and polar coordinate system respectively. The origin of each system is located at O.

$$\text{position } P_1 = \begin{cases} x_1 = f \sin\theta \cos\varphi \\ y_1 = f \sin\theta \sin\varphi \\ z_1 = -f \cos\theta \end{cases}, \quad \begin{cases} f^2 = x_1^2 + y_1^2 + z_1^2 \\ r_1^2 = x_1^2 + y_1^2 \end{cases} \quad (1.23)$$

$$\text{position } P_2 = R = \begin{cases} x_2 = r_2 \cos\Psi \\ y_2 = r_2 \sin\Psi \\ z_2 \end{cases}, \quad r_2^2 = x_2^2 + y_2^2 \quad (1.24)$$

The unit vector s can be written as

$$s = \sin\theta \cos\varphi \hat{x} + \sin\theta \sin\varphi \hat{y} + \cos\theta \hat{z} \quad (1.25)$$

The \hat{x} , \hat{y} and \hat{z} are unit vectors in x, y and z direction, then the Eq. (1.22) can rewritten as

$$E(r_2, \Psi, z_2) =$$

$$\frac{i}{\lambda} \iint_{\Omega} E_0(\theta, \varphi) \exp[-ikr_2 \sin\theta \cos(\varphi - \Psi) - ikz_2 \cos\theta] \sin\theta d\theta d\varphi \quad (1.26)$$

Considering the refraction of the wave on A-A' plane, as shown in Fig 1-5 the $P(r)$ is converted to $P(\theta)$, then, Eq. (1.21) become

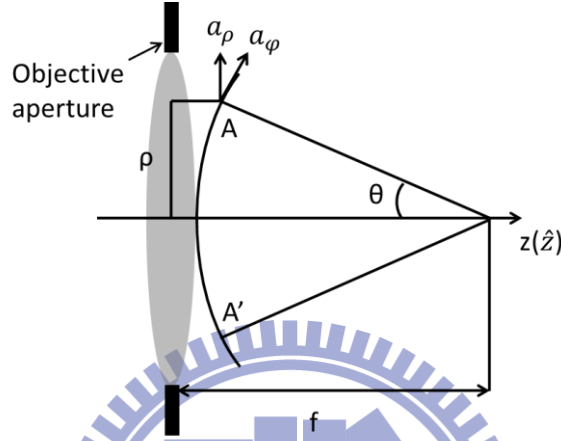


Fig. 1-5 A side view of the generalized optical system.

$$\begin{aligned} E_0(\theta, \varphi) = E_i(\theta, \varphi) = P(\theta) \cos\varphi a_\rho - P(\theta) \sin\varphi a_\varphi = \\ P(\theta) \{ [\cos\theta + \sin^2\varphi(1 - \cos\theta)] \hat{x} \\ + \cos\varphi \sin\varphi (\cos\theta - 1) \hat{y} + \cos\varphi \sin\theta \hat{z} \} \end{aligned} \quad (1.27)$$

We substitute Eq. (1.27) into the Eq. (1.26), leading to

$$E(r_2, \Psi, z_2) =$$

$$\begin{aligned} \frac{i}{\lambda} \iint_{\Omega} P(\theta) \{ [\cos\theta + \sin^2\varphi(1 - \cos\theta)] \hat{x} + \cos\varphi \sin\varphi (\cos\theta - 1) \hat{y} \\ + \cos\varphi \sin\theta \hat{z} \} \exp[-ikr_2 \sin\theta \cos(\varphi - \Psi) - ikz_2 \cos\theta] \sin\theta d\theta d\varphi \end{aligned} \quad (1.28)$$

The integration with respect to φ is from 0 to 2π and θ is from 0 to α , then the electromagnetic wave in the focal region of an objective can be expressed as

$$E(r_2, \Psi, z_2) = \frac{\pi i}{\lambda} \{ [I_0 + \cos(2\Psi) I_2] \hat{x} + \sin(2\Psi) I_2 \hat{y} + 2i \cos\Psi I_1 \hat{z} \} \quad (1.29)$$

The definition of three variables I_0 , I_1 and I_2 is given by

$$I_0 = \int_0^\alpha P(\theta) \sin\theta (1 + \cos\theta) J_0(kr_2 \sin\theta) \exp(-ikz_2 \cos\theta) d\theta \quad (1.30)$$

$$I_1 = \int_0^\alpha P(\theta) \sin^2\theta J_1(kr_2 \sin\theta) \exp(-ikz_2 \cos\theta) d\theta \quad (1.31)$$

$$I_2 = \int_0^\alpha P(\theta) \sin\theta (1 - \cos\theta) J_2(kr_2 \sin\theta) \exp(-ikz_2 \cos\theta) d\theta \quad (1.32)$$

Where the J_0 , J_1 and J_2 are the zero-order, first-order and second-order Bessel functions of the first kind.

Eq. (1.29) shows the fields distribution in focal region of a higher numerical aperture objective has three components even though the incident light is only one component. We can find the vectorial properties of light can be described by vectorial Debye theory, but not in scalar diffraction theory.

1.2.2 Fresnel's equations

The Fresnel's equations discussed the reflection and transmission coefficient with different polarization in this situation, a plane wave is incident from medium 1 onto the interface to medium 2 under an incident angle θ_i . If the electric field is tangential to the interface, the electromagnetic wave is called s-polarization; the orthogonal polarization is called p-polarization, as shown in Fig 1-6 (a) and (b).

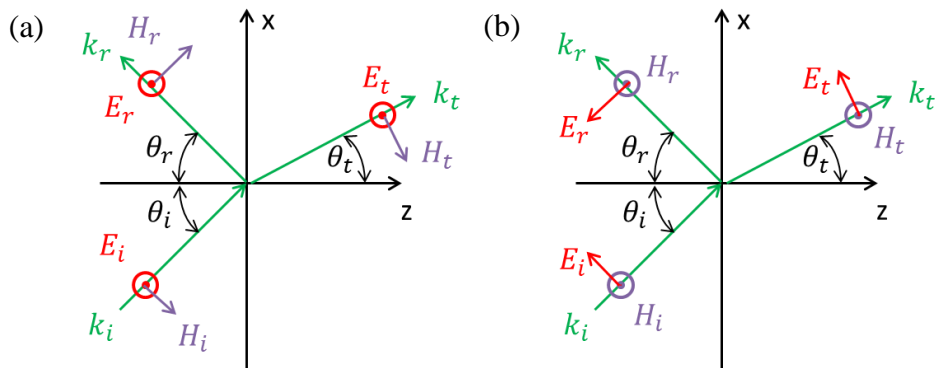


Fig. 1-6 Geometry of Fresnel's equations for (a) s-polarization and (b) p-polarization.

For s-polarization, the tangential incident fields are

$$\begin{aligned} E_{iy} &= t_s \exp[in_i k_0 (x \sin \theta_i + z \cos \theta_i)] \\ H_{ix} &= -\frac{n_i k_0}{\omega \mu} \cos \theta_i E_{iy} \end{aligned} \quad (1.33)$$

The reflected fields are

$$\begin{aligned} E_{ry} &= r_s \exp[in_i k_0 (x \sin \theta_i - z \cos \theta_i)] \\ H_{rx} &= \frac{n_i k_0}{\omega \mu} \cos \theta_i E_{ry} \end{aligned} \quad (1.34)$$

And the transmitted fields are

$$\begin{aligned} E_{ty} &= t_s \exp[in_t k_0 (x \sin \theta_t - z \cos \theta_t)] \\ H_{tx} &= \frac{n_t k_0}{\omega \mu} \cos \theta_t E_{ty} \end{aligned} \quad (1.35)$$

Requiring the continuity of fields at the interface, we can obtain

$$\begin{aligned} 1 + r_s &= t_s \\ n_i \cos \theta_i - r_s n_i \cos \theta_i &= t_s n_t \cos \theta_t \end{aligned} \quad (1.36)$$

Then a non-magnetic medium was assumed. The solution is

$$\begin{aligned} r_s &= \frac{n_i \cos \theta_i - n_t \cos \theta_t}{n_i \cos \theta_i + n_t \cos \theta_t} \\ t_s &= \frac{2n_i \cos \theta_i}{n_i \cos \theta_i + n_t \cos \theta_t} \end{aligned} \quad (1.37)$$

The calculation for p-polarization is similar,

$$\begin{aligned} r_p &= \frac{n_t \cos \theta_i - n_i \cos \theta_t}{n_t \cos \theta_i + n_i \cos \theta_t} \\ t_p &= \frac{2n_i \cos \theta_i}{n_t \cos \theta_i + n_i \cos \theta_t} \end{aligned} \quad (1.38)$$

1.2.2 Jones calculus

Jones Calculus including matrix and vector operation is a quantitatively mathematical description of polarization state. The polarization states can describe by

a vector, called the Jones vector, and each polarization optical element has associated Jones matrix. Then the optical system can be described by multiplication with the corresponding Jones vector and Jones matrix. If we have an linear polarized normal incident beam which includes $E_x = A \exp[i(-\omega t + kz)]$, the Jones vector of the electric fields is

$$\vec{E} = \begin{bmatrix} E_x \\ E_y \end{bmatrix} = A e^{i(kz - \omega t)} \begin{bmatrix} 1 \\ 0 \end{bmatrix} \xrightarrow{\text{normalized}} \begin{bmatrix} 1 \\ 0 \end{bmatrix} \quad (1.39)$$

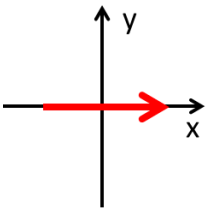
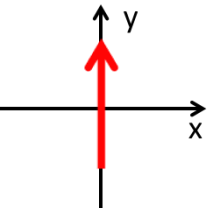
Where A and B are amplitude, for convenience of computation, the time-dependent term is ignored and then we denote the Jones vector into normalized forms.

When putting an polarization optical component, the state of polarization transfer from $[E_x \ E_y]$ into $[E'_x \ E'_y]$, the optical component is represented by Jones matrix.

$$J' = \begin{bmatrix} E'_x \\ E'_y \end{bmatrix} = \begin{bmatrix} a & b \\ c & d \end{bmatrix} \begin{bmatrix} E_x \\ E_y \end{bmatrix} = MJ \quad (1.40)$$

Where J is the Jones vector of incident beam, J' is the Jones vector emergent beam, and M is the Jones matrix.

Table 1.1 and Table 1.2 show some general examples of Jones vector and Jones matrices.

Polarization	Jones vector	Illustration
Linear in x-direction	$\begin{bmatrix} 1 \\ 0 \end{bmatrix}$	
Linear in y-direction	$\begin{bmatrix} 0 \\ 1 \end{bmatrix}$	

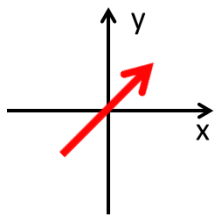
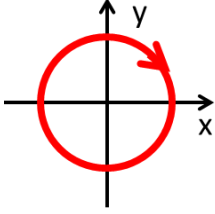
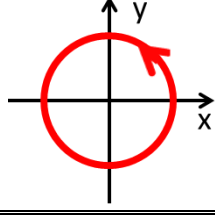
Linear at 45°	$\frac{1}{\sqrt{2}} \begin{bmatrix} 1 \\ 1 \end{bmatrix}$	
Right circular	$\frac{1}{\sqrt{2}} \begin{bmatrix} 1 \\ -i \end{bmatrix}$	
Left circular	$\frac{1}{\sqrt{2}} \begin{bmatrix} 1 \\ i \end{bmatrix}$	

Table 1-1 The reference between polarization and Jones vector.

Optical element	Jones matrix
Neutral element	$\begin{bmatrix} 1 & 0 \\ 0 & 1 \end{bmatrix}$
x-polarizer	$\begin{bmatrix} 1 & 0 \\ 0 & 0 \end{bmatrix}$
y-polarizer	$\begin{bmatrix} 0 & 0 \\ 0 & 1 \end{bmatrix}$
Quarter-wave retarder	$\begin{bmatrix} 1 & -i \\ -i & 1 \end{bmatrix}$
Half-wave retarder	$\begin{bmatrix} 0 & 1 \\ 1 & 0 \end{bmatrix}$

Table 1-2 The reference between optical elements and Jones matrices.

1.3 Comparison of two diffraction theory

Through the discussion of scalar and vector diffraction theory, respectively, we can find out some differences as following:

1. The vector diffraction theory is able to completely describe polarization of light,

but scalar diffraction theory cannot.

2. The thickness of obstacle is assumed as zero in scalar diffraction theory, but it must be taken into account in vector diffraction theory.
3. The scalar diffraction theory is only an approximation; therefore, that entails some degree of error.

1.4 Motivation & Organization

Recently, the optical engineering is rapidly developed. More and more parameters of light and material properties should be taken into consideration due to the dimension of interested area is gradually reduced. Therefore, the scalar diffraction theory is not suitable anymore; the vector diffraction theory is the only way to get accurate solution. Polarization is also an important property of light in vector diffraction theory; the different polarizations of light can elicit different effects in material. Through the vector diffraction theory, we can observe the phenomenon of interaction between light and material, and discuss the influence of polarization of light in focus fields of light. Consequently, we hope we can obtain some useful applications utilize the influence of polarization of light in this thesis.

This thesis will be partitioned into three major parts, first part of this thesis talks about the effect of polarization in different numerical aperture in chapter 2, the influence of polarization is more distinct when numerical aperture is bigger. It will be demonstrated in later.

The second part is the first application of polarization which called extended depth of focus; it is achieved through the synthesis of two orthogonal polarizations or higher order of inhomogeneous polarization. It will discuss in chapter 3. The third part is the second application of polarization which is utilized to excited polychromatic surface plasmon resonance, the system and synthesis method will be

introduced in chapter 4.

Finally, the conclusions and future works will be described in chapter 5.



Chapter 2

Polarization Beams

The mode of the electric field vibration is called “polarization”. According to the beam with the same polarization at every point within the pupil plane or not, the polarization beam can divide into homogeneous and inhomogeneous. In this chapter, the focal field properties of two kinds of polarization will be shown in following.

2.1 Homogeneous and inhomogeneous polarization

Homogeneous polarization keep the identical polarization at every point within the pupil plane; we can describe the field distribution by using the function dependent on the ratio of electric field. If the beam only has the x-component of electric field, it is called x-directional linear polarization. If the phase delay between x-component and y-component is 90° , the polarization is called circular polarization.

As the standard operation process is not homogeneous among the pupil, it is inhomogeneous polarization beam. The obvious difference can observe from Fig. 2-1

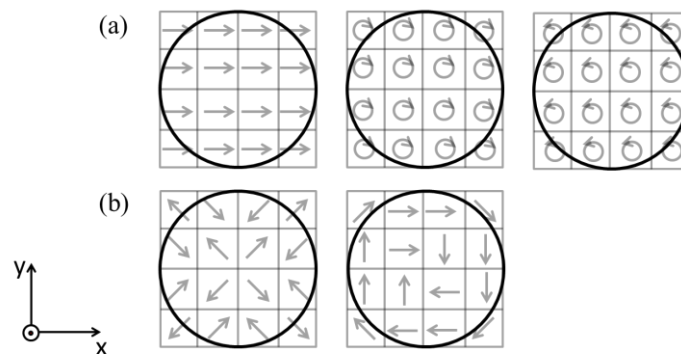


Fig. 2-1 (a) and (b) illustrates the homogeneous and in homogeneous beam, respectively.

One typical spatially inhomogeneous beams is the cylindrical vector beams,

which attracted much attention due to its symmetric feature. The general solution of the wave equation for cylindrical vector beams includes two solutions: radially polarized beam and azimuthally polarized beam. The orthogonal cylindrical vector beams have the doughnut-shaped irradiance and good symmetry in r -direction or ϕ -direction. Due to the good symmetry, the radially polarized beam is p-polarization in omni-direction at the incident plane; likewise, the azimuthally polarized is s-polarization, as shown in Fig. 2-2. Then the focused field distribution properties of different polarization with different numerical aperture will be discussed in following.

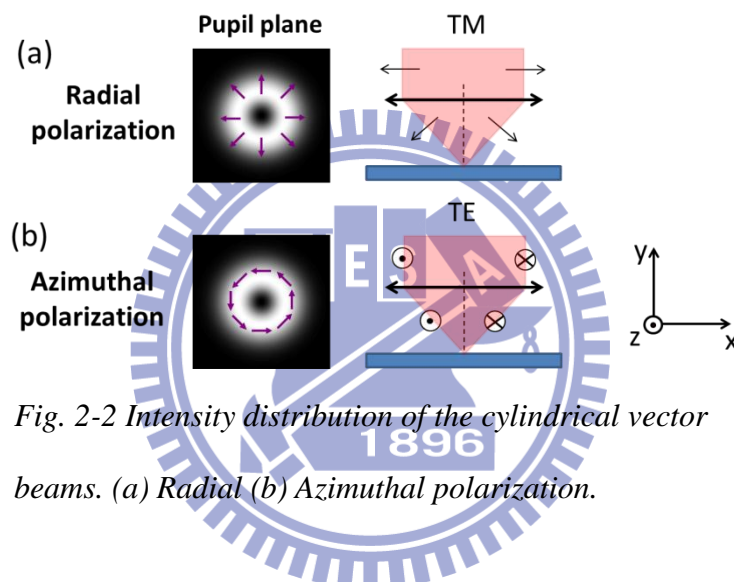


Fig. 2-2 Intensity distribution of the cylindrical vector beams. (a) Radial (b) Azimuthal polarization.

2.2 Properties of polarized beam

In this section, the polarization states at the entrance pupil are linear, circular, radial, and azimuthal, respectively. Examples of focal distribution with different numerical aperture foci are shown.

2.2.1 Linear polarization

Considering an entrance pupil in which the polarization is x-direction linear polarized and constant amplitude. The focused field distribution is circular symmetry for small numerical aperture, when numerical aperture increases, it become

asymmetrical field which is larger along the direction of polarization due to the electric field of z-components is no longer negligible in high numerical aperture, as shown in Fig. 2-3. Therefore, the focused field is reduced which yields a broader focus when numerical aperture is larger than 0.7. This is a direct result of the vector effect.

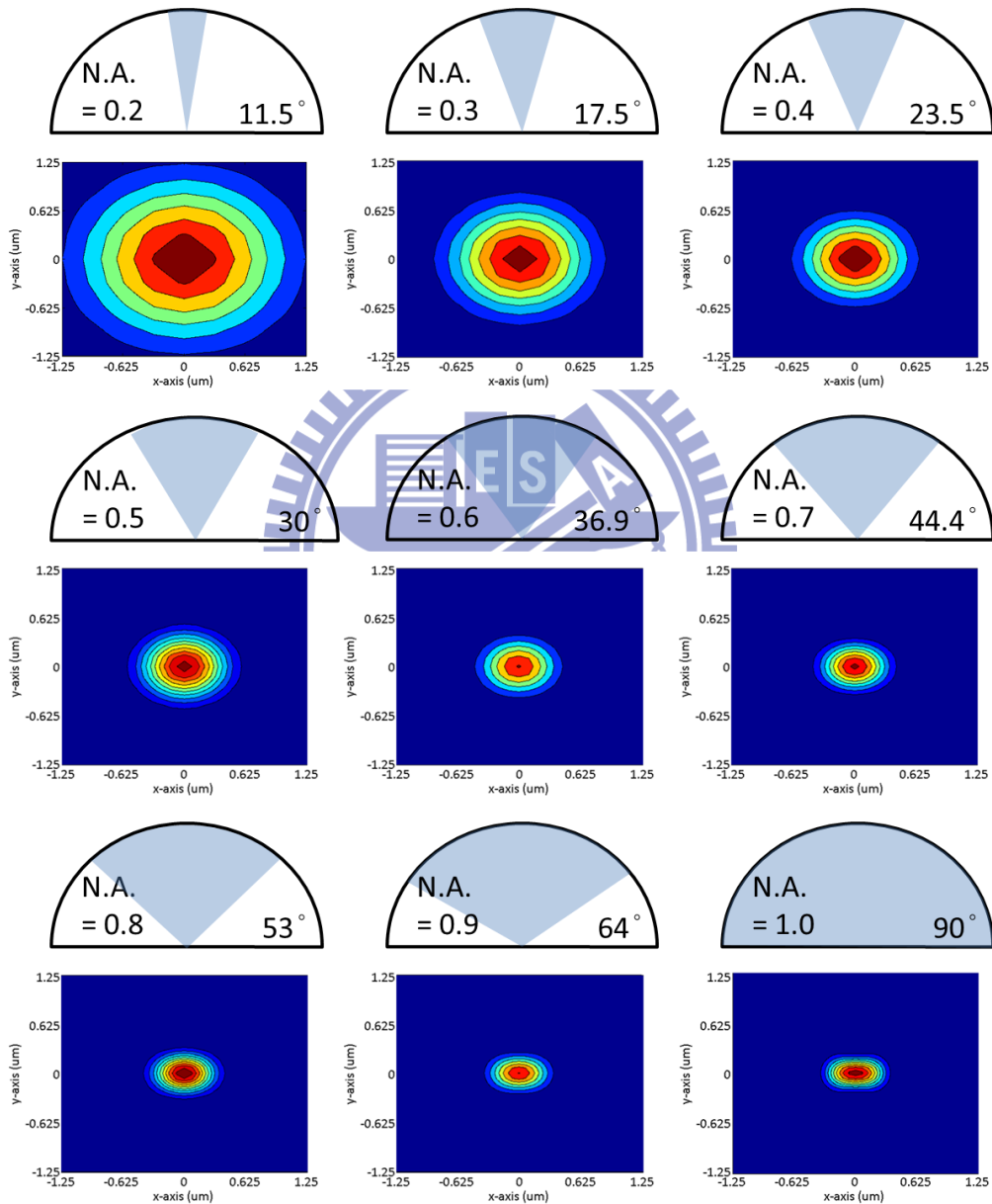


Fig. 2-3 Intensity profile of linearly polarized focus as numerical aperture increases from 0.2 to 1.0, where the vectorial feature becomes more apparent with high-NA system.

2.2.2 Circular polarization

Now, considering an entrance pupil in which the polarization is right circular polarized and constant amplitude. The focused field distribution is circular symmetry no matter small or high numerical aperture, as shown in Fig. 2-4. Because of the electric field of z-component has circular symmetry in the doughnut-shaped and vanished on the optical axis. The x and y component are both asymmetrical but with orthogonal axes, so the sum of each components is symmetrical.

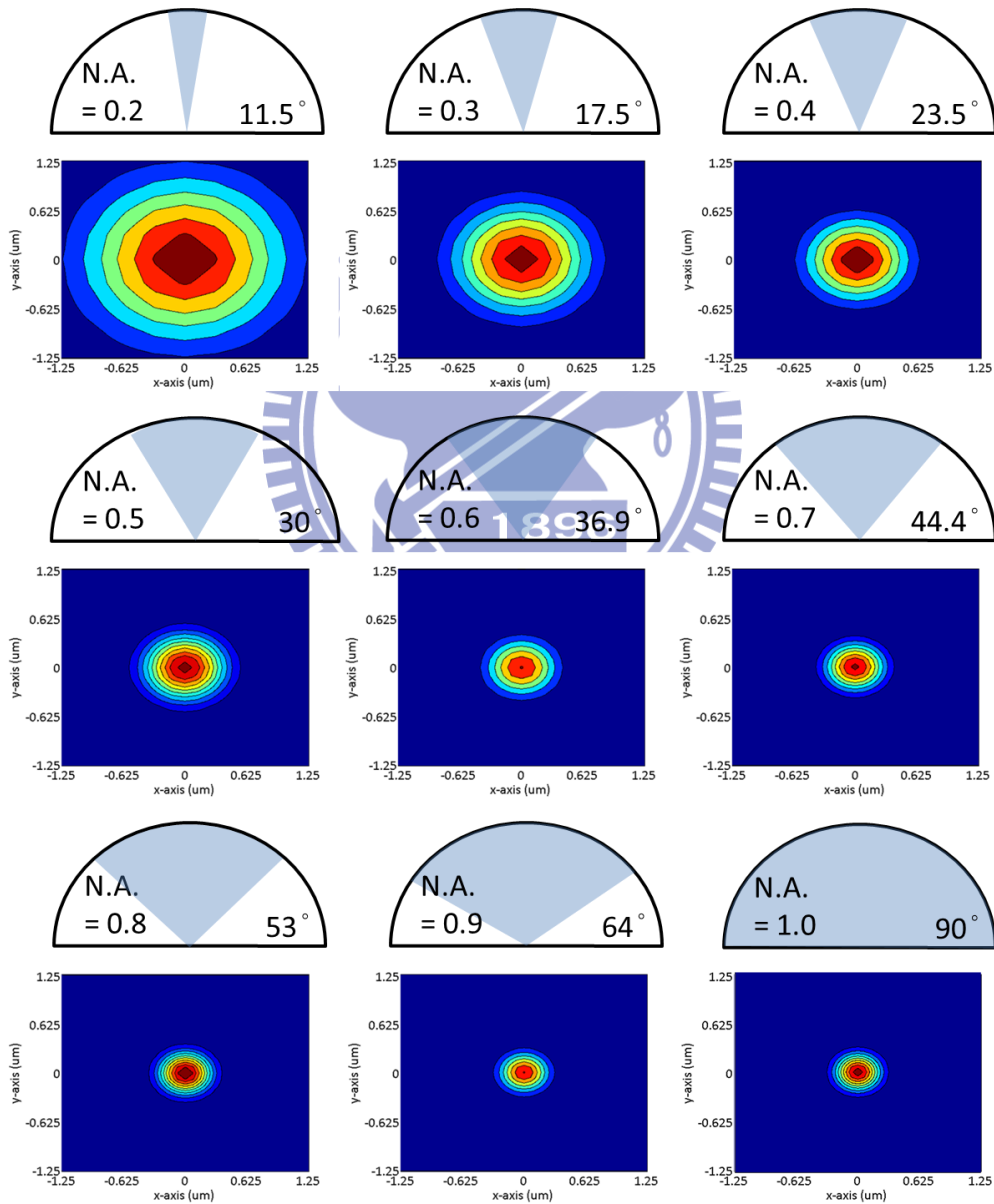
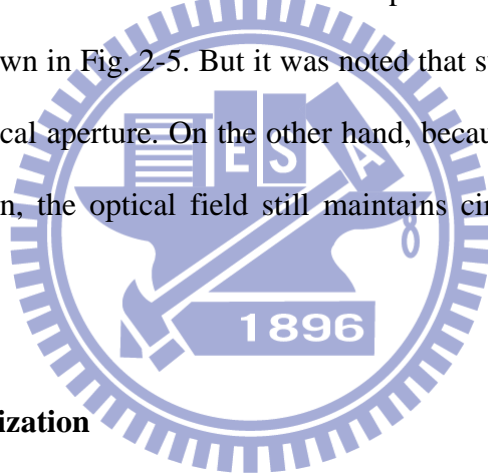


Fig. 2-4 Intensity profile of circular polarized focus for increasing numerical aperture.

2.2.3 Radial polarization

For aforementioned polarization, their amplitude is constant, but for a radially polarized pupil, amplitude forms a donut-shaped field because of the singularity in the center. When numerical aperture is larger than 0.7, the optical field is transformed from a doughnut-shaped to a flat-topped shape due to the depolarization effect starts to govern the shape of the focused spot. Then the focused field of radially polarized beams has a sharp intensity peak because of the strong depolarization effect which caused the constructive interference of the z-component. Compared with linear polarization and circular polarization, the smaller spot obtained from radial polarization was under the conditions of numerical aperture larger than 0.9 and 0.95, respectively [3], as shown in Fig. 2-5. But it was noted that superior illumination only exists in a high numerical aperture. On the other hand, because of the good polarized symmetry in r-direction, the optical field still maintains circular symmetry for any numerical aperture.



2.2.4 Azimuthal polarization

Azimuthal polarization is similar to radial polarization; the amplitude cannot be constant and forms a donut-shaped field because of the singularity in the center and due to the good polarized symmetry in ϕ -direction, the optical field also maintains circular symmetry for any numerical aperture. The special focused feature of azimuthal polarization is that yields a doughnut-shaped field even when numerical aperture is larger than 0.7, as shown in Fig. 2-6. The reason of the special focused field is that adjacent parts of this polarization are π -phase shifted with each other, respectively. And another special focused feature is that electric field of z-component is zero, therefore, the azimuthal polarization created an optical cage with the absence of z-component electric field at the vicinity of focal point, as shown in Fig. 2-7.

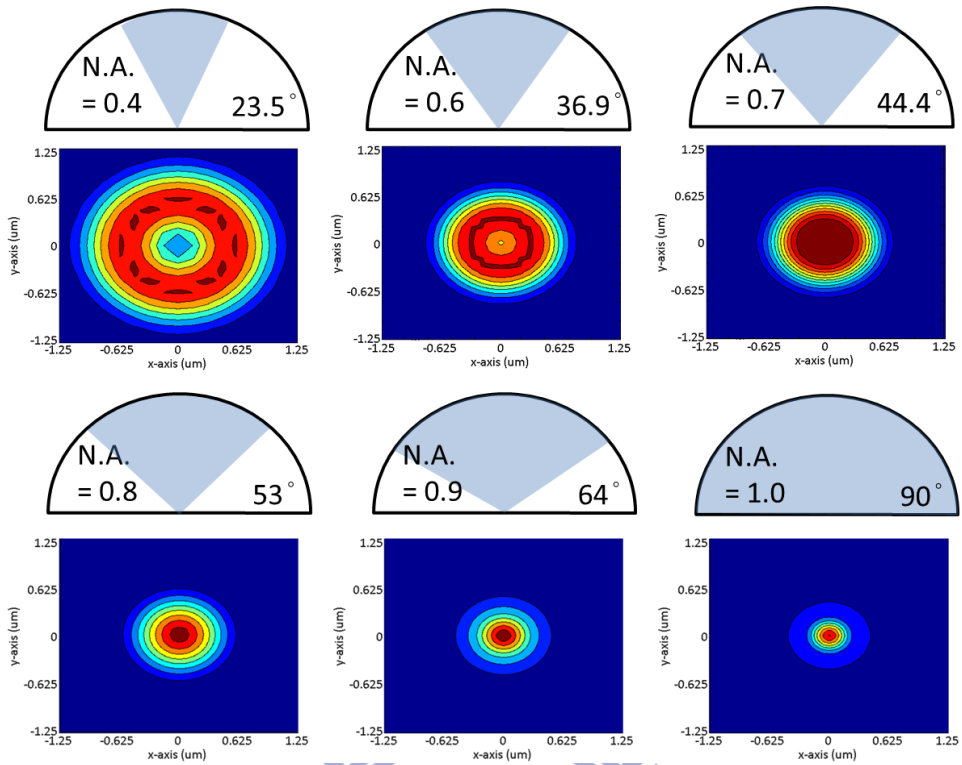


Fig. 2-5 Intensity profile of radially polarized beams in different numerical aperture. When numerical aperture increased, the optical field is transformed from a doughnut-shaped to a flat-topped shape.

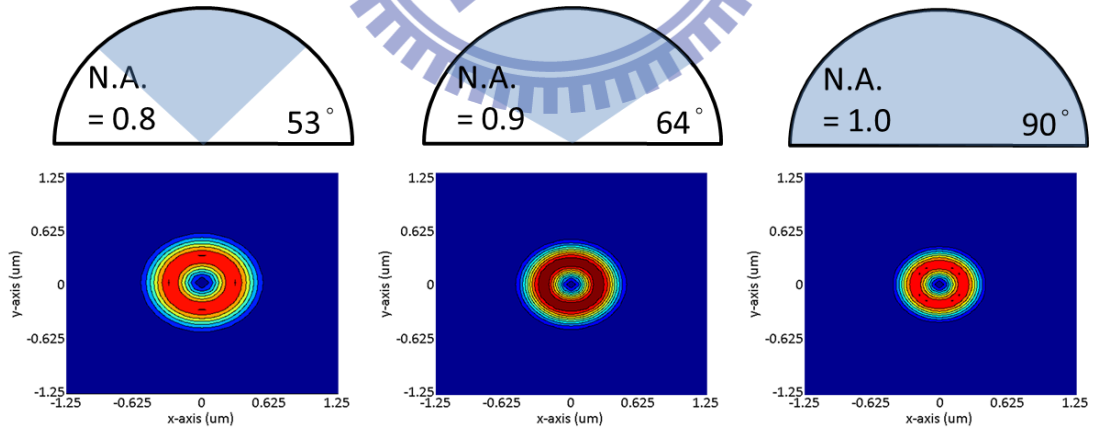


Fig. 2-6 Focused intensity profile of azimuthally polarized beams for high numerical aperture.

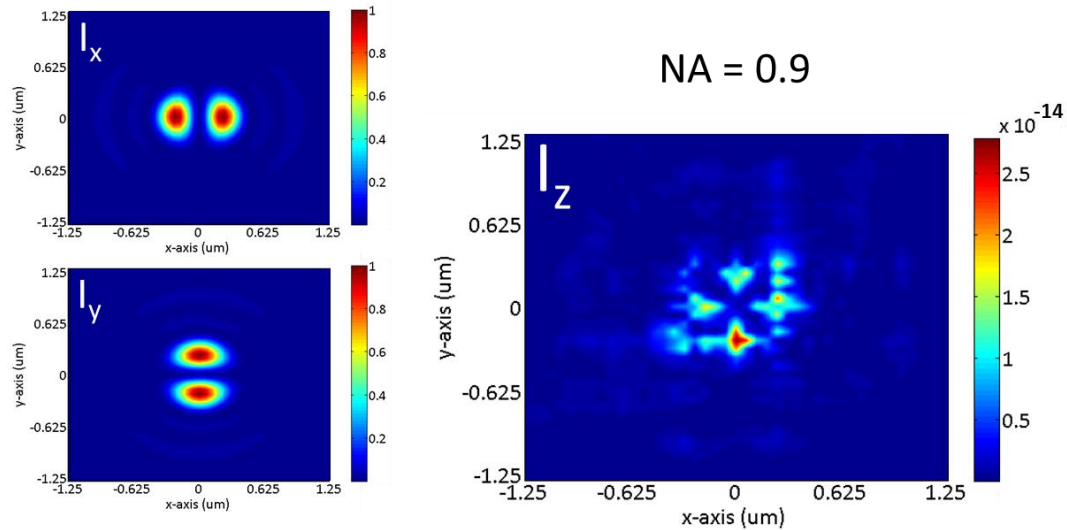


Fig. 2-7 Each component of focal fields in azimuthally polarized light, due to the destructive interference of depolarization effect, the electric field of z-component is zero.

2.3 Summary

The general solution with homogeneous and inhomogeneous polarization has been discussed in aforementioned statement, respectively. Through the aforesaid discussion, we can find out the homogeneous polarization is not suitable in high numerical aperture system in terms of bigger focal spot size or changed shape of focused fields which results from vector effect. For inhomogeneous polarization, due to the depolarization effect in high numerical aperture, radial polarization could be focused tighter beyond the diffract limits. It can further improve the resolution and be applied to particle acceleration [4,5], particle-trapping [6], lithography [7], and material processing [8]. On the other hand, because of the specific phase distribution of azimuthal polarization, it can generate a sharper focal spot which smaller than the focal spot of linear polarization when it propagates through a vortex $0-2\pi$ phase plate [9]. As a consequence, inhomogeneous polarization becomes more important in many application of optics.

Chapter 3

Application 1 – Extended Depth of Focus

It is well known that imaging systems are sensitive to defocus error. Since 1950s, many groups made an attempt reduce the sensitivity of defocusing by extending the depth of focus. In this chapter, we will introduce a novel polarization coding technique without post signal processing.

3.1 History and Principle

From the view of wave optics, the defocusing aberration produces finite depth of focus (DoF) because it introduces an additional quadratic phase in the pupil function of the imaging system, resulting in a spatial low-pass filter effect. We will demonstrate in following.

The optical transfer function (OTF) of a single-lens imaging system can be written as a autocorrelation of the pupil function $P(x, y)$.

$$H(f_x, f_y) = \frac{\iint_{-\infty}^{\infty} P(x + \frac{\lambda z_i f_x}{2}, y + \frac{\lambda z_i f_y}{2}) P^*(x - \frac{\lambda z_i f_x}{2}, y - \frac{\lambda z_i f_y}{2}) dx dy}{\iint_{-\infty}^{\infty} |P(x, y)|^2 dx dy} \quad (3.1)$$

Where f_x, f_y are the spatial frequencies, λ is the wavelength of light, and z_i is the distance from the lens to image plane. For a circular pupil, when defocusing aberration is considering, the generalized pupil function will leads to the form

$$P(x, y) = |P(x, y)| \exp[ikW(x, y)] \quad (3.2)$$

Where $k = 2\pi/\lambda$, and $W(x, y)$ is the aberration function of defocusing, it has the quadratic form

$$W(x, y) = W_m \frac{(x^2 + y^2)}{b^2} \quad (3.3)$$

Where b is the radius of the aperture, and the number W_m is a convenient indication of

the severity of the defocusing error, is given by

$$W_m = \frac{b^2}{2} \left(\frac{1}{z_i} + \frac{1}{z_o} - \frac{1}{f} \right) \quad (3.4)$$

Where z_o is the distance from the object to the lens and f is the focal length of the lens.

When the imaging condition is not fulfilled (W_m is not zero), the OTF distribution is narrower due to the quadratic phase factor arises. For the 1-D case Eq. (3.1) become

$$\begin{aligned} H(f_x, W_m) &= \frac{\int_{-\infty}^{\infty} P \left(x + \frac{\lambda z_i f_x}{2} \right) P^* \left(x - \frac{\lambda z_i f_x}{2} \right) dx}{\int_{-\infty}^{\infty} |P(x)|^2 dx} \\ &= \frac{\int_{A(f_x)} \exp \left[\frac{ikW_m 2\lambda z_i f_x x}{b^2} \right] dx}{2b} \end{aligned} \quad (3.5)$$

Where $A(f_x)$ is the 1-D overlap between two shifted pupil functions. Then Eq. (3.5) gives the 1-D OTF

$$H(f_x) = \left(1 - \frac{|f_x|}{2f_c} \right) \text{sinc} \left[\frac{8W_m \pi}{\lambda} \left(\frac{f_x}{2f_c} \right) \left(1 - \frac{f_x}{2f_c} \right) \right] \quad (3.6)$$

Where $f_c = \frac{b}{\lambda z_i}$, when W_m is large value and the value of f_x is not too large in comparison to f_c , that $A(f_x)$ can be approximated by $A(0)$, where $A(0)$ is the total area of the pupil. Then the OTF can be approximated by

$$\begin{aligned} H(f_x) &\approx \frac{\int_{A(0)} \exp \left[\frac{ikW_m 2\lambda z_i f_x x}{b^2} \right] dx}{2b} \\ &= \frac{\int_{-b}^b \exp \left[\frac{ikW_m 2\lambda z_i f_x x}{b^2} \right] dx}{2b} \\ &= \frac{1}{2b} \int_{-\infty}^{\infty} \text{rect} \left(\frac{x}{2b} \right) \exp \left[\frac{ikW_m 2\lambda z_i f_x x}{b^2} \right] dx \\ &= \text{sinc} \left(\frac{4W_m \pi z_i f_x}{b} \right) \end{aligned} \quad (3.7)$$

The expression of Eq. (3.7) demonstrates that defocusing aberration results a low-pass filtering effect.

In order to reduce the effect of defocusing, various methods were investigated

for overcome this limitation. In 1952, E. H. Linfoot and E. Wolf [10] computed the complete out-of-focus airy pattern for annular apertures and incidentally found out the DoF was increased, then 1960, W. T. Welford [11] investigate the phenomenon in depth; this is the earliest and simplest method to reduce the defocusing aberration. Due to the DoF is inverse proportion to pupil area, hence, through addition of binary blocking mask in aperture plane, the DoF can be extend. The influence of additional annular ring on total intensity field can be described mathematically

$$I(z) = \frac{a^4}{\lambda^2 f^2} \left\{ \frac{\sin \left[\frac{1}{2} p (1 - \varepsilon^2) \right]}{\frac{1}{2} p} \right\}^2, p = \pi a^2 z / \lambda f^2 \quad (3.8)$$

Where a is radius of aperture, f is the distance from the exit pupil to the focus, and the ε is obstruction ratio of radius as shown in Fig. 3-1.

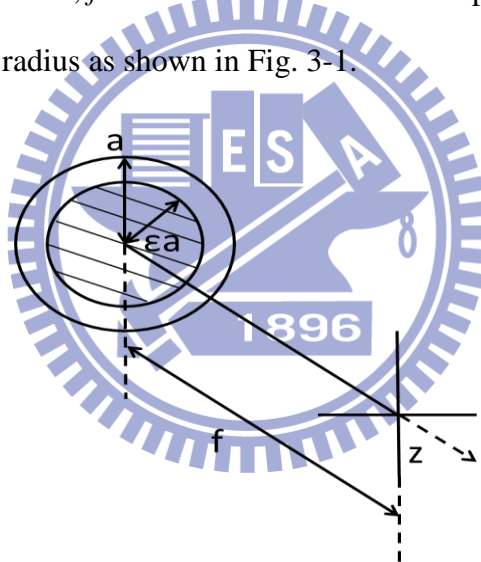


Fig. 3-1 The configuration for annular aperture.

We can find out the total intensity field which does not change with different position when ε is tending to unity. It means that DoF will extend to infinite, but unfortunately when ε is larger, the side-lobe intensity of light fields and the obstructive area will arise. Therefore, the system resolution and amount of light reaching the imaging plane is lower.

Another approach uses the refractive elements (Axicon) in the aperture of the imaging

system [12,13]. An extended DoF is obtained due to the overlap region of beams being diverted by refractive elements. As illustrated in in Fig. 3-2.

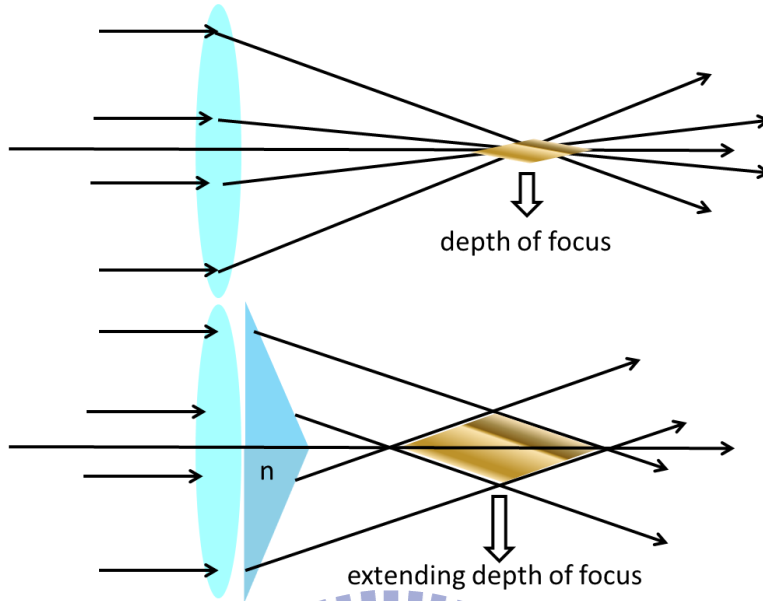


Fig. 3-2 The schematically concept of extending depth of focus by refractive optics.

Recently, because the computer develops vary rapidly; it brings another technique which is called wave-front coding elements to extend depth of focus [14]. This method is not an all-optical approach due to that requires digital post-processing, the idea involves that inserting a basically aberration which is much stronger than the defocusing aberration such that by digital post-processing a sharp image can be reconstructed.

One of the popular elements is the cubic phase element, in normalized coordinates; the pupil function with cubic phase element is given by

$$P(x) = \begin{cases} 1/\sqrt{2} \times \exp(iax^3) & \text{for } |x| \leq 1 \\ 0 & \text{otherwise} \end{cases} \quad (3.9)$$

Where a is the coefficient which controls the phase deviation. Then the OTF related to the pupil function can be approximated as

$$H(f_x, W_m) \approx \left(\frac{\pi}{12|\alpha f_x|} \right)^{1/2} \exp\left(i \frac{\alpha f_x^3}{4}\right) \exp\left(i \frac{k^2 W_m^2 f_x}{3\alpha}\right), u \neq 0 \quad (3.10)$$

When α is a larger value, the third part of the approximated of the OTF can be ignored, therefore, the OTF will be independent of defocusing. Although this type of solution can increased DoF plenty but rather one that requires digital post-processing, thus it does not fit to ophthalmic. In addition to cubic phase mask, there are still some another mask, i.e. free-form phase mask and exponential phase mask. [15,16]

Then, a novel polarization coding technique will be introduced in following.

3.2 Combination of inhomogeneous beams

After realizing these methods which extending DoF utilize amplitude manipulation or phase manipulation. In this section, we describe a novel inhomogeneous polarization coding aperture to achieve extending DoF. In 2006, Wanli Chi *et al* purposed this novel technique by combining two independent orthogonal linear polarized lights [17]. As shown in Fig. 3-3, it has been demonstrated the effect which can extend DoF before. But in chapter 2, we already discuss the properties with homogeneous and inhomogeneous light; the inhomogeneous polarized light is superior to linear polarized light in terms of focus spot size or influence of polarized direction in higher numerical aperture. Therefore, maybe we can not only extend DoF but also increase the resolution by combing radial and azimuthal polarized lights.

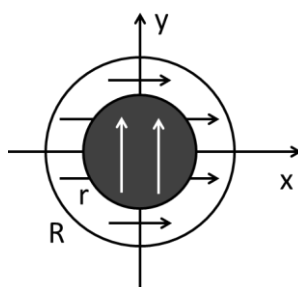


Fig. 3-3 The polarization coded aperture.

In the combination with radially and azimuthally polarized light, there are two kinds of synthesis, as shown in Fig. 3-4. Manipulating the proportion between radially and azimuthally polarized light, we can find out the best ratio to obtain maximum of extending DoF. In Fig. 3-5 (a) to Fig. 3-5 (j), the radially polarized light is in outer ring region and the central circular region is azimuthally polarized light. The opposite arrangement of two polarized light is showed in Fig. 3-6 (a) to Fig. 3-6 (j). The numerical number of system in here is 1.45.

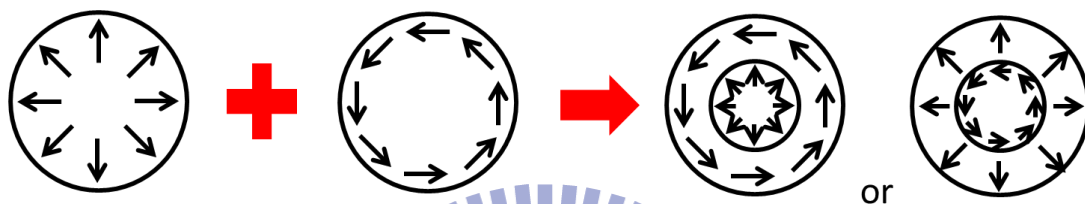


Fig. 3-4 Two types of radial and azimuthal combination.

According to figures 3-4, we can find out the shape of light field is determined by the polarization at outer ring region. The syntheses of two orthogonal polarizations actually have the capability to extend depth of focus. The best combinative ratio of radially polarized light to azimuthally polarized light is 3:7 when radially polarized light is at the outer ring region. On the other hand, when azimuthally polarized light is at the outer ring region, the ratio of radially polarized light to azimuthally polarized light is 7:3; the results can obtain from Fig. 3-5(g) and Fig. 3-6 (g). In Fig. 3-7, we discuss the full width at half maximum (FWHM) in z-axis of the two kind of best combination, Fig. 3-7 (a) and (b) shows the slice of focus fields on z-axis, and FWHM is 1.48 times and 1.7 times comparing combination and non-combination, respectively. However, although the inhomogeneous polarization coded aperture can extend depth of focus, but one of the aperture cannot obtain more better resolution than linear polarization coded aperture and the extend efficiency of these kinds aperture are not

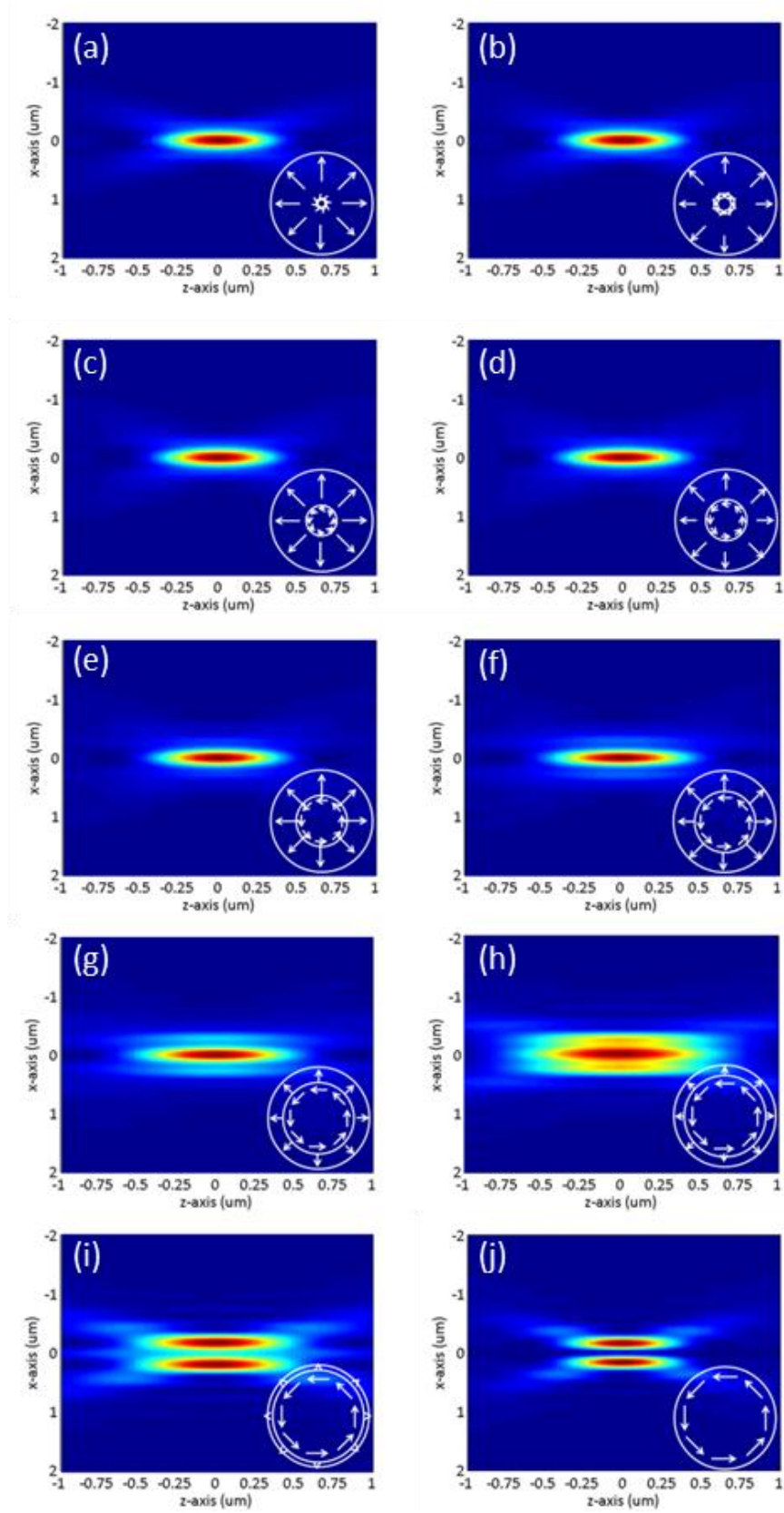


Fig. 3-5 (a) to (j) peak intensity across different z -axis position when radially polarized light is in outer ring region.

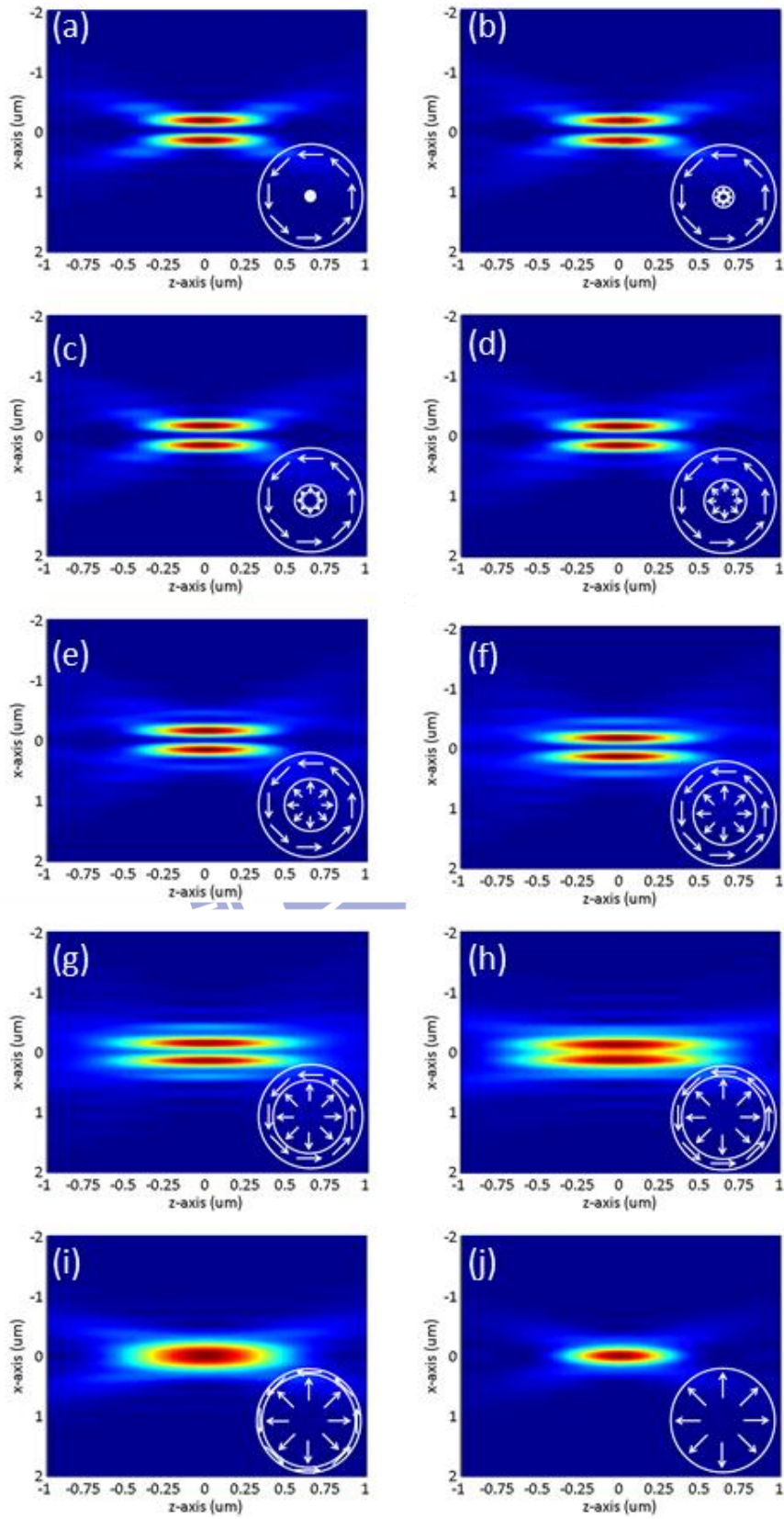


Fig. 3-6 (a) to (j) peak intensity across different z -axis position when azimuthally polarized light is in outer ring region.

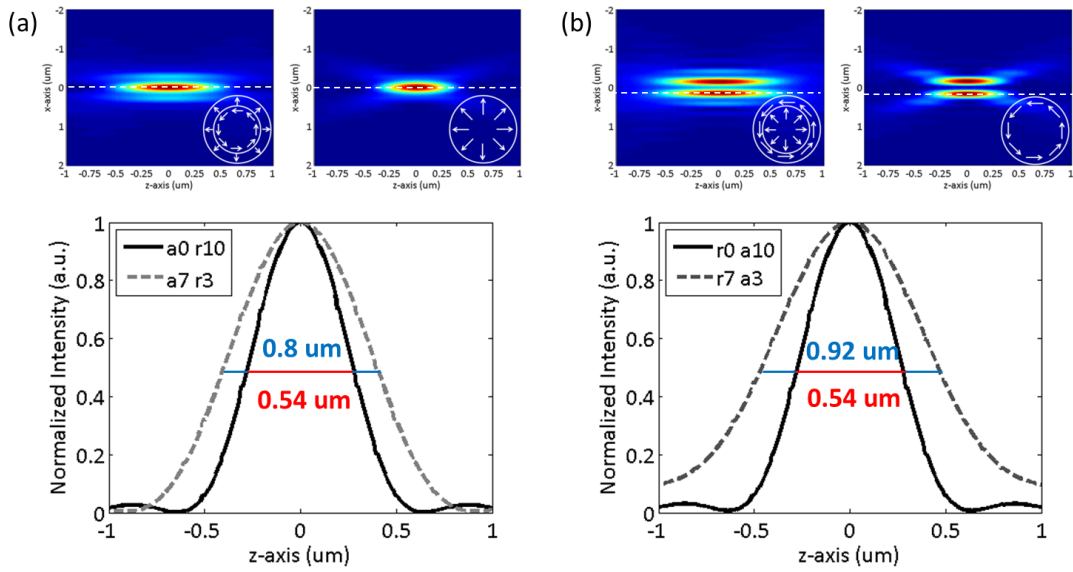


Fig. 3-7 The FWHM of (a) radially polarized light and (b) azimuthally polarized light focal fields.

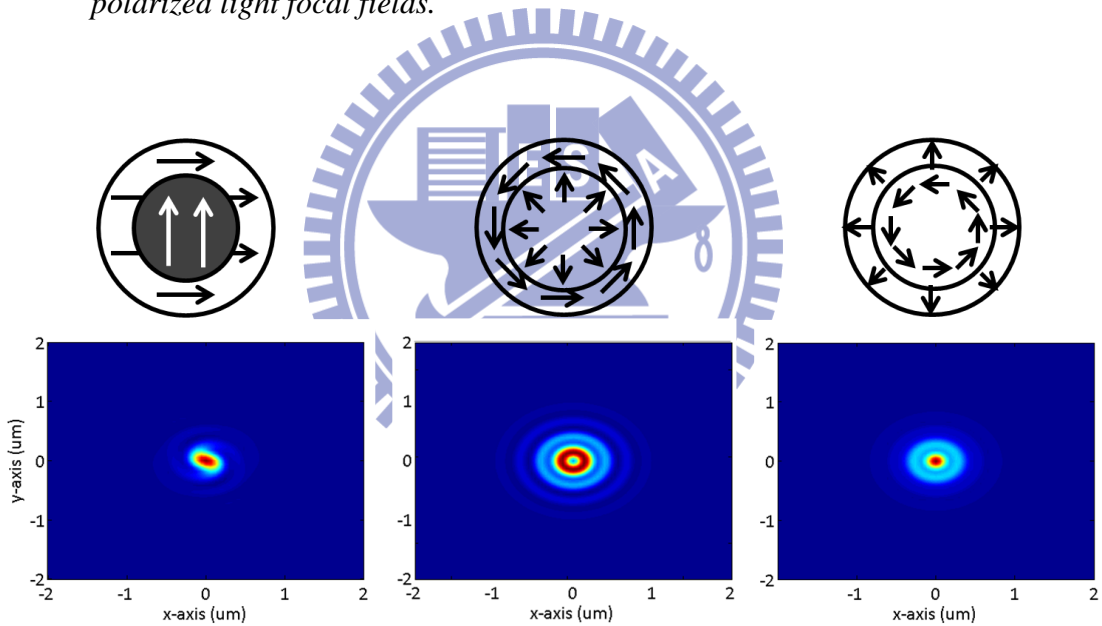


Fig. 3-8 The intensity profile comparison between linear polarization coded aperture and in homogeneous coded aperture on x-y dimension.

good enough, as shown in Fig. 3-8. Therefore, we consider the depolarization effect of radially polarized light again, to obtain the good extended depth of focus due to depolarization effect in higher-order radially polarized light.

3.3 Higher-order radially polarized beam

In chapter 2, we already discussed the properties of fundamental mode of radially polarized beam in terms of its strongly longitudinal component which results by depolarization effect forms a tight focal spot in high numerical aperture system. For this reason, recently, the higher-order radially polarized beam have been attracted much attention due to it can effectively reduce the focal spot size by destructive interference on horizontal components[18], it means that the higher-order radially polarized beam can produce a smaller focal spot size than fundamental mode in high numerical aperture system. Therefore, in this section, we utilized the higher-order radially polarized beam to achieve not only super-resolution but also extending DoF. Since that very high longitudinal component has been achieved nearly flat top axial distribution in focal volume.

The order number of radially polarized beam depends on how many ring it has. Single-ring-shaped beam is called fundamental mode radially polarized beam ($R-TEM_{01}$), and so on, double-ring-shaped beam is the first order of higher-order radially polarized beam which called $R-TEM_{11}$, as shown in Fig. 3-9. Here, we compare the focus fields on z -axis between fundamental mode and two higher-order modes.

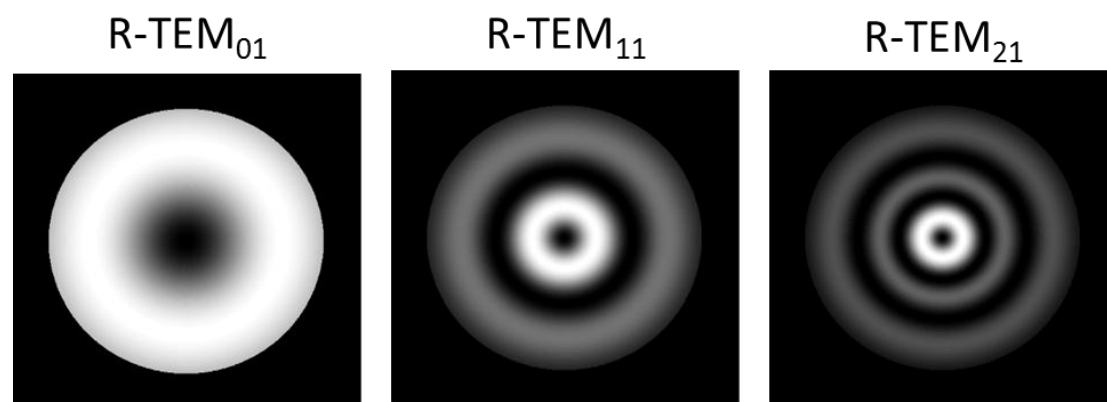


Fig. 3-9 The fundamental mode ($R-TEM_{01}$) and two higher-order modes ($R-TEM_{11}$ and $R-TEM_{21}$) of radially polarized beam.

In Fig. 3-10, it shows the ability of extended DoF with higher-order radially polarized beam, compare to fundamental modes (R-TEM₀₁), the FWHM is 1.7 times and 2.11 times in R-TEM₁₁ and R-TEM₂₁, respectively. Of cause, the better results can be expected when the more higher-order to be chosen.

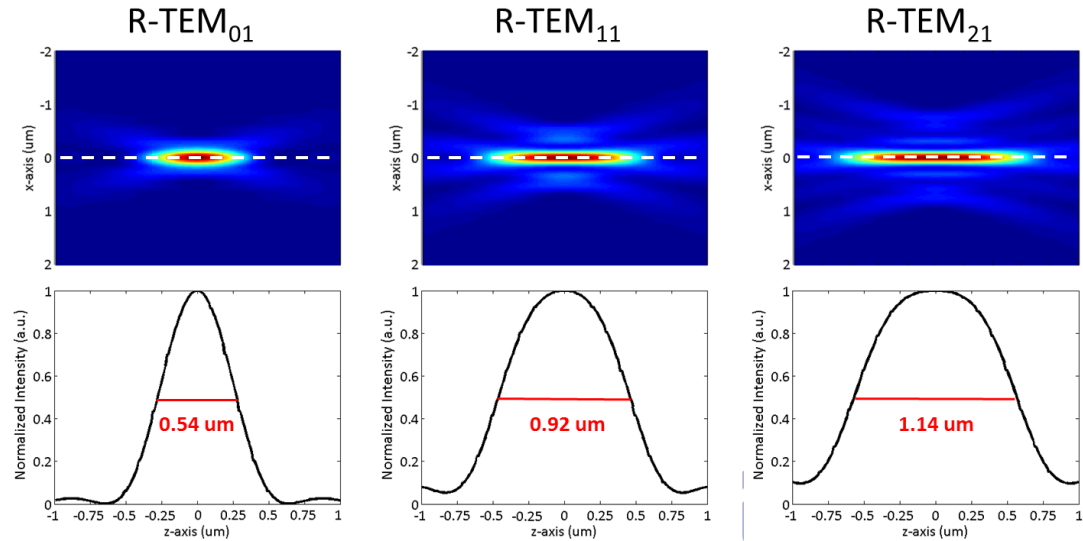


Fig. 3-10 The FWHM of focal fields of different order of radially polarized beam.

Although the higher-order radially polarized beam has many advantages, but it has a vital constraint that the synthesis of higher-order beams is difficult to achieve. Up to now, the strategy to generates higher-order radially polarized beam is nothing more than through spatial light modulator (SLM) [19] or particular laser cavity design [20,21], but these synthesis methods are sensitivity to environment perturbation or precise manufacture. Therefore, the practical application of higher-order still has a barrier to prevent the development.

3.4 Summary

In this chapter, we introduce two recipes of polarization coded to extend DoF; one is the combination between radial polarization and azimuthal polarization, and the other is the higher-order radially polarized beam. Employing the advantages of

cylindrical vector beam, we can achieve high spatial resolution as well as extended DoF in high numerical aperture system.



Chapter 4

Application 2 – Chromatic Surface Plasmon Resonance

Recently, surface plasmon resonance (SPR) have been widely used to analyze characteristics of material, providing quantitative and qualitative analyses due to its unique character. In this chapter, the experimental setup for creating the chromatic SPR and the optimized structure for objective-based configuration will be introduced in the following.

4.1 History and Principle

The discovery of SPR begins at 1902, R. W. Wood observed a weird phenomenon that didn't obey the diffraction theorem of grating when the polarization of light with electric field upright to the groove of metal grating [22]. He attempted to explain the phenomenon by oscillation with specific polarization of light and metal grating structure. Until 1941, Fano purposed a new opinion about the interesting phenomenon, he proposed a new electromagnetic wave along the surface when the polarization of light with electric field upright to the groove of metal grating [23]. The electromagnetic wave is so-called SPR afterward. Then in 1950, R. H. Ritchie and R. A. Ferrell *et al* purposed the theoretic model of SPR sequentially [24, 25], From then on, SPR elicited the interests of scientist, more attention invested in this study.

The SPR are collective oscillations of free electrons that can propagate between the metal and dielectric surface. It is a kind of electromagnetic wave and confined within the sub-wavelength of metal surface. Exactly as above said, the SPR are electromagnetic wave, therefore, we can find the condition of existence of SPR from Maxwell's equation. In order to know the condition, we consider an interface between two media and look for a homogeneous solution of Maxwell's equations at the surface.

The Maxwell's equation at the surface between two media can be written as

$$\nabla \times \vec{H} = \varepsilon \frac{d\vec{E}}{dt} \quad (4.1a)$$

$$\nabla \times \vec{E} = -u \frac{d\vec{H}}{dt} \quad (4.1b)$$

$$\nabla \cdot \varepsilon \vec{E} = 0 \quad (4.1c)$$

$$\nabla \cdot \vec{H} = 0 \quad (4.1d)$$

Next considering s-polarization and p-polarization incident waves propagate between two media as shown in Fig. 4-1, for s-polarization incident wave, the wave function is

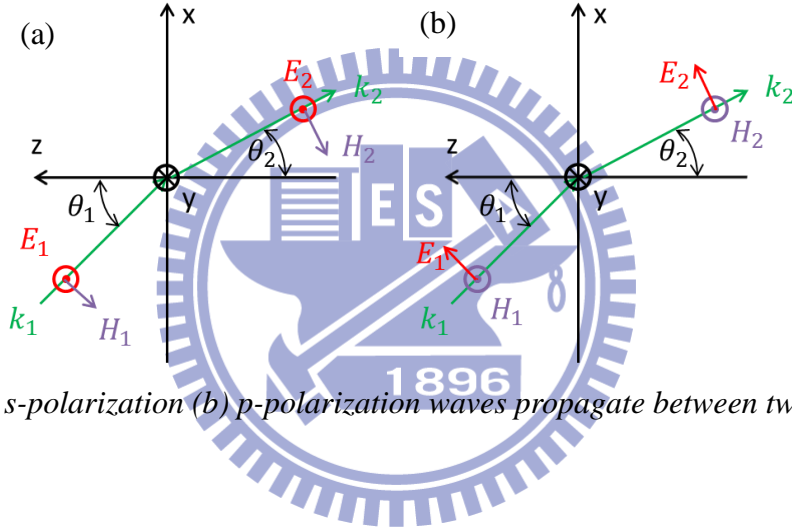


Fig. 4-1 (a) s-polarization (b) p-polarization waves propagate between two media.

$z > 0$

$$\vec{H}_1 = (H_{x1}, 0, H_{z1}) \exp(k_{x1}x + k_{z1}z - \omega t)i \quad (4.2a)$$

$$\vec{E}_1 = (0, E_{y1}, 0) \exp(k_{x1}x + k_{z1}z - \omega t)i \quad (4.2b)$$

$z < 0$

$$\vec{H}_2 = (H_{x2}, 0, H_{z2}) \exp(k_{x2}x - k_{z2}z - \omega t)i \quad (4.2c)$$

$$\vec{E}_2 = (0, E_{y2}, 0) \exp(k_{x2}x - k_{z2}z - \omega t)i \quad (4.2d)$$

From Eq. (4.2a) to Eq. (4.2d), these equations must satisfy boundary condition, then electric fields and magnetic fields at the surface are of the form

$$E_{y1} = E_{y2} \quad (4.3a)$$

$$u_1 H_{z1} = u_2 H_{z2} \quad (4.3b)$$

$$H_{x1} = H_{x2} \quad (4.3c)$$

$$k_{x1} = k_{x2} \quad (4.3d)$$

Substituting Eq. (4.2a) to Eq. (4.2d) into Eq. (4.1b) leads to

$$k_{z1} E_{y1} = -u_1 \omega H_{x1} \quad (4.4a)$$

$$-k_{z2} E_{y2} = -u_2 \omega H_{x2} \quad (4.4b)$$

$$k_{x1} E_{y1} = -u_1 \omega H_{z1} \quad (4.4c)$$

$$k_{x2} E_{y2} = -u_2 \omega H_{z2} \quad (4.4d)$$

For nonmagnetic materials, $u_1 \approx u_2$, according as Eq. (4.3a) to Eq. (4.3d), we can obtain a result of wave-vector

$$k_{z1} = -k_{z2} \quad (4.5)$$

Comparing with dispersion relation

$$k_{x1}^2 + k_{z1}^2 = \varepsilon_1 \left(\frac{\omega}{c}\right)^2 \quad (4.6a)$$

$$k_{x2}^2 + k_{z2}^2 = \varepsilon_2 \left(\frac{\omega}{c}\right)^2 \quad (4.6b)$$

We can know that Eq. (4.5) is contradiction if $\varepsilon_1 \neq \varepsilon_2$ from Eq. (4.6). That because the s-polarization wave only has electron field along the surface, so there are no electron accumulation. Hence, the SPR for s-polarization don't exist at the surface, in other words, the s-polarization incident wave cannot excite the SPR

For p-polarization incident wave, the wave function is

$z > 0$

$$\vec{H}_1 = (0, H_{y1}, 0) \exp(k_{x1}x + k_{z1}z - \omega t)i \quad (4.7a)$$

$$\vec{E}_1 = (E_{x1}, 0, E_{z1}) \exp(k_{x1}x + k_{z1}z - \omega t)i \quad (4.7b)$$

$z < 0$

$$\vec{H}_2 = (0, H_{y2}, 0) \exp(k_{x2}x - k_{z2}z - \omega t)i \quad (4.7c)$$

$$\vec{E}_2 = (E_{x2}, 0, E_{z2}) \exp(k_{x2}x - k_{z2}z - \omega t)i \quad (4.7d)$$

From Eq. (4.7a) to Eq. (4.7d), these equations must satisfy boundary condition, then electric fields and magnetic fields at the surface are of the form

$$H_{y1} = H_{y2} \quad (4.8a)$$

$$E_{x1} = E_{x2} \quad (4.8b)$$

$$\varepsilon_1 E_{z1} = \varepsilon_2 E_{z2} \quad (4.8c)$$

$$k_{x1} = k_{x2} \quad (4.8d)$$

Due to the symmetric of propagating wave at the interface, $E_{z1} = -E_{z2}$, then relation of permittivity between two media is

$$\varepsilon_1 = -\varepsilon_2 \quad (4.9)$$

The significance of Eq. (4.9) indicated the SPR only exist and are excited on metal which is negative index. Then Substituting Eq. (4.7a) to Eq. (4.7d) into Eq. (4.1a) leads to

$$k_{z1}H_{y1} = \varepsilon_1\omega E_{x1} \quad (4.10a)$$

$$k_{x1}H_{y1} = -\varepsilon_1\omega E_{z1} \quad (4.10b)$$

$$k_{z2}H_{y2} = -\varepsilon_2\omega E_{x2} \quad (4.10c)$$

$$k_{x2}H_{y2} = \varepsilon_2\omega E_{z2} \quad (4.10d)$$

$$\frac{k_{z1}}{\varepsilon_1} + \frac{k_{z2}}{\varepsilon_2} = 0 \quad (4.10e)$$

Finally, from Eq. (4.10e) and Eq. (4.8d) it leads to dispersion relation

$$k_{x1} = k_{spp}(\omega) = \frac{\omega}{c} \sqrt{\frac{\varepsilon_1(\omega)\varepsilon_2(\omega)}{\varepsilon_1(\omega) + \varepsilon_2(\omega)}} \quad (4.11a)$$

$$k_{zi} = \sqrt{\varepsilon_i k_0^2 - k_{x1}^2} \quad i = 1, 2 \quad (4.11b)$$

In order to excite the SPR, we require that k_{x1} is real and k_{zi} is purely imaginary in

both media. Then permittivity of both media only can be

$$\varepsilon_1 + \varepsilon_2 < 0 \quad (4.12)$$

$$\varepsilon_1 \cdot \varepsilon_2 < 0 \quad (4.13)$$

The significance of Eq. (4.13) and Eq. (4.12) is similar to Eq. (4.9), which means that not only either index of two media must be negative, but also the absolute value of negative index exceeding that of the other. Most of the materials, especially noble metals have large negative real part of dielectric constant. Therefore, the SPR can exist at the interface between a noble metal and a dielectric when the polarization of incident light is p-polarization.

After realized the condition of existence of SPR, we can find out only p-polarization light can excite SPR on the interface between metal and dielectric, so recently, radially polarized light has been widely used to excite SPR due to the good axial symmetric of p-polarization, and the merits of radially polarized light in terms of a tighter focal spot already confirm in many investigations [26, 27]. But current technology does not allow for a simply frequency sweeping operation system for radially polarized light. These major issues delay the progress on the development of SPR and hinder further study on wavelength dependent material. Therefore, how to simply create the white light radially polarized light and build up a polychromatic radially polarized surface plasmon resonance (PC-RPSPR) sensor will be shown up in following section.

4.2 Experimental Setup

The experimental setup of PC-RPSPR sensor can divide into two principal parts, first part is synthesis of radially polarized white light utilized an approach of spatially varying polarizer (SVP), as shown in Fig. 4-2 (a), and second part is the metal-insulator-metal (MIM) structure for extending sensing range on sensor system.

We utilize an unpolarized white LED (model: Luxeon Star/O LXHL-NWE8) as a light source which has advantages of low cost and is speckle free. A collimated unpolarized light was converted to radially polarized light by the use of SVP. The radially polarized white light then relays to the entrance pupil of the commercial immersion objective lens (Olympus PlanApo-N 60x/1.45 Oil). Its corresponding half divergence angle is 75.16° , well beyond the SPR resonant angle $\theta_{SP} \sim \pm 45^\circ$ at wavelength $\lambda_0 = 610 \text{ nm}$. After passing through the objective, the white light focus on the MIM structure, Non-coupled reflected light has been collected and guides backward into two different optical paths via the same objective lens. One optical path projected the reflected intensity distribution onto CCD image sensor from the back focal plane of the objective lens. The other optical path records the spectra of reflected beam via a spectrum analyzer. As shown in Fig. 4-2.

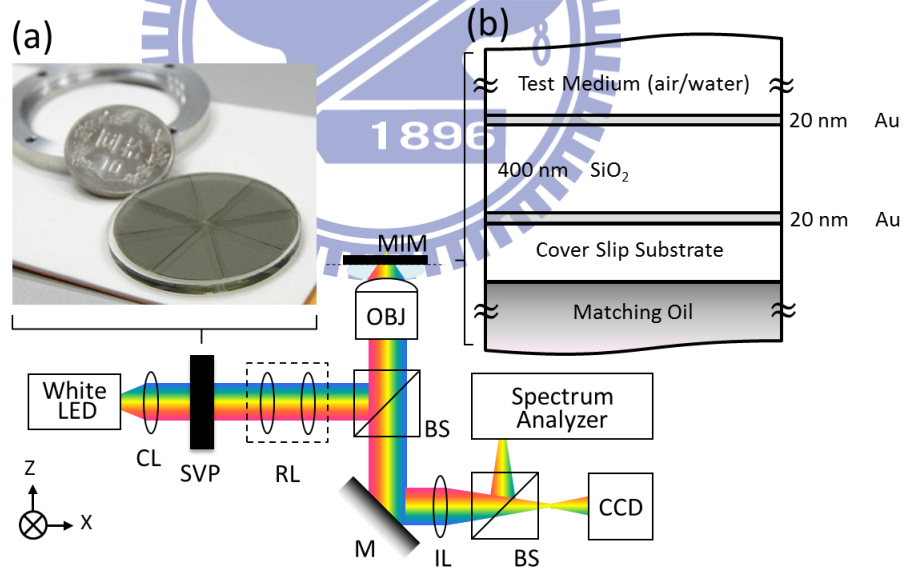


Fig. 4-2 Configuration of the PC-RPSPR sensor, where CL: collimated lens, SVP: spatial varying polarizer, RL: relay lens, BS: beam splitter, M: mirror, IL: image lens, MIM: metal-insulator-metal structure. The insets show (a) the photo of SVP, (b) the schematic diagram of MIM structure.

4.2.1 Synthesis of polychromatic radially polarized light

The SVP consists of eight pieces of linear polarizer and the transmission axis of every sector aligned to individual principle radial direction, as shown in Fig. 4-3. The SVP is used to convert unpolarized white light into radially polarized white light. In microscopies, nano-optics, and spectroscopy, polychromatic radially polarized beams can supply other perspectives. Based on past reported studies, the common recipe to synthesis or generate radial polarization are designed for a specific working wavelength and rely on the use of phase element, liquid crystal, interference configuration [28, 29, 30, 31]. Those elements are wavelength dependent. This means that it cannot operate universally among different working wavelength in a fixed design. However, only few numbers of devices can generate those kinds of light in recently. The main systems are double conical reflector system which based on geometrical optics [32] and fiber-based system [33]. Unfortunately, the former system create a discontinuous ring beam shape, which decreases the resolution due to the increment of side-lobe part in focal region and seems difficult to be apply for sensing; the latter system need the procedure of precise optical alignment to couple incident light into fiber. In other words, these systems are not simply and convenient. On the contrary, proposed SVP is assembled by conventional polarizing element offering wavelength independent properties for polarization conversion and simplify the creative complexity of system. Also, it has a compact size with extremely low cost, but this device exchanges those benefits for power consumption.

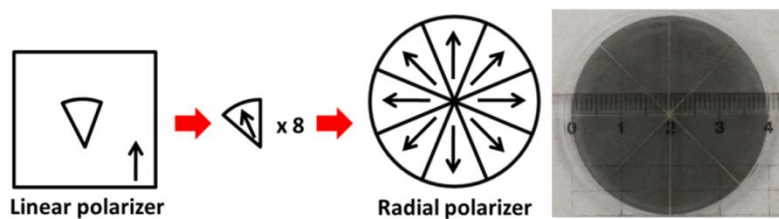


Fig. 4-3 The SVP assembly, which is composed of eight sectors.

4.2.2 MIM Structure

The MIM structure ($\lambda_0 = 610$ nm) is glass ($\varepsilon = 2.126$) / 20 nm Au ($\varepsilon = -8.5 + 2.02i$) / 400 nm SiO₂ ($\varepsilon = 2.126$) / 20 nm Au ($\varepsilon = -8.5 + 2.02i$) sandwiched between matching oil ($\varepsilon = 2.29$) and a test sample (Air or Water), as shown in Fig. 4-2 (b).

The function of the MIM structure is used to extend the sensing range of refractive index for test sample up to about 1.42. According to the excitation mechanism of SPR, the incidence angle, which provides sufficient wave-vectors to agree phase matching conditions, is greater than the critical angle. The SPR angle is wavelength dependent and is related to the dispersion relation of metal. Its resonance angle shifts up when working wavelength decreased. Furthermore, generally the refractive index of living cells are close to water ($\theta_{\text{SPR, water}} \sim 77.4^\circ$, $\lambda_0 = 610$ nm) which beyond the sensing limit for objective lens with NA = 1.45 ($\theta_{\text{max}} \sim 75.16^\circ$, $\lambda_0 = 610$ nm). Under this circumstance, the SPR dips are outside the observation windows as the wavelength is smaller than 640 nm as shown in Fig. 4-4. Therefore, the MIM structure is purposed,

As the beam focused on the MIM structure, not only cavity resonance (CR) modes but also transformed surface plasmon resonance (T-SPR) modes which have broader sensing range are generated. CR modes are insensitive to the change of the refractive index of sample, but T-SPR mode is. The role of a MIM structure is to transform generated cavity resonance (CR) modes into transformed surface plasmon resonance (T-SPR) modes. The material and thickness of each layer determine the resonance property of both modes. In order to maximum the depth of surface plasmon resonant dips, we kept the symmetry property of MIM structure and set the overall thickness of gold thin film as 40 nm, also, in order to confirm the effect of MIM structure, we chose SiO₂ as insulator which is identical to substrate. In our case, when the dip of CR modes exceeded the critical angle, the CR modes would yield abundant

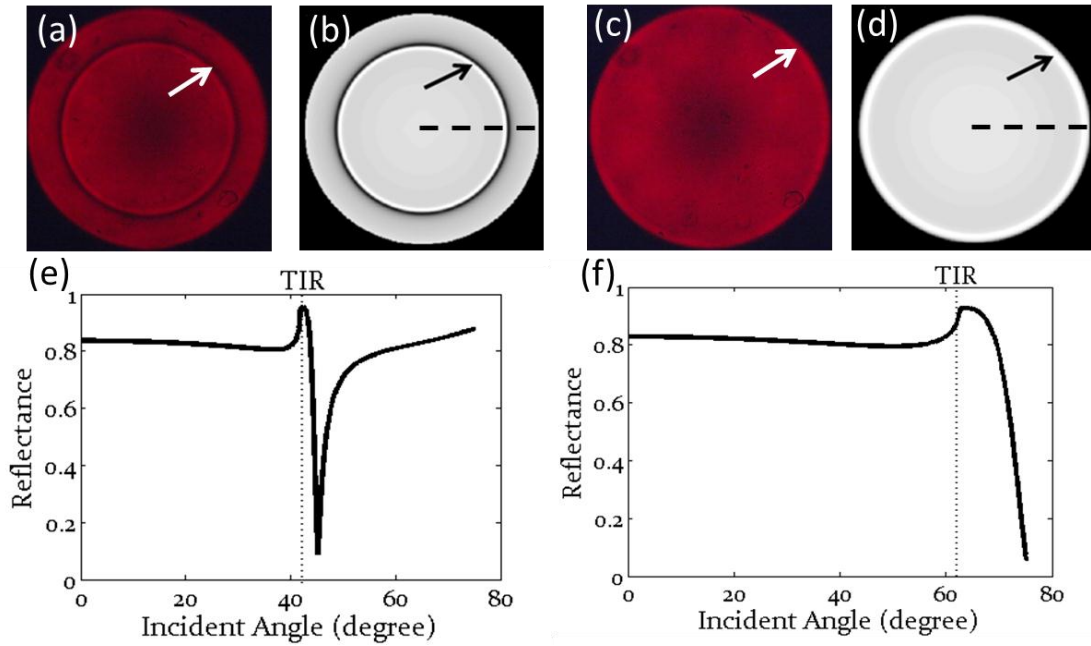


Fig. 4-4 Comparison with the different test sample. (a) and (c) are experimental data and (b) and (d) are simulation when test sample is air and water, respectively. (e) and (f) are the slice of (b) and (d), respectively. The wavelength here is 610 nm.

evanescent waves. Then, the energy of evanescent wave would be transferred to a new SPR which can be excited by smaller propagating constant, because MIM structure [the thickness of insulator should be larger than 100 nm (150 nm) @ $\lambda = 450$ nm when test sample is chosen to be air (water)] supports an additional SPR solution in the dispersion relation diagram. As a result, this T-SPR mode provides the capability to detect sample with higher refractive index at the same incident angle, it also have obviously angular shift and linear dependence in sensitivity, as shown in Fig. 4-5. Thus, this new angle-to-angle mappings function extended the sensing range of the refractive index up to $n \sim 1.42$ which is beyond typical range of living cells.

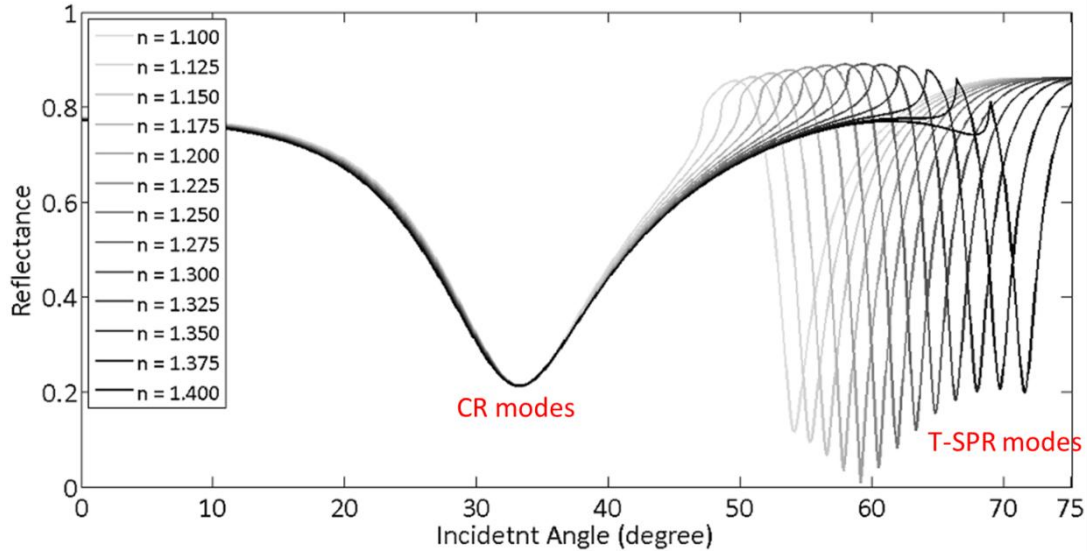


Fig. 4-5 Obviously angular shift in T-SPR modes by comparing the different refractive index of test sample.

4.3 Matrix method

After realizing the function of MIM structure, the matrix method will be introduced to simulate the efficiency of MIM structure.

Using the matrix method is facilitated to track the complex amplitudes of the forward and backward waves through the boundaries of multilayer structure. Consider two waves propagating on both sides of dielectric interface. The electric fields can be written as

$$E_1 = (A_1 e^{ik_{x1}x} + B_1 e^{-ik_{x1}x}) e^{ik_{z1}z} \quad \text{medium 1} \quad (4.14a)$$

$$E_2 = (A_2 e^{ik_{x2}x} + B_2 e^{-ik_{x2}x}) e^{ik_{z2}z} \quad \text{medium 2} \quad (4.14b)$$

Where A_1 and A_2 are the amplitudes of right-traveling wave which propagated along +x direction, and B_1 and B_2 are the amplitudes of left-traveling wave which propagated along -x direction. Solving the relationship between A_1 , B_1 , A_2 , and B_2 in a matrix form, we can obtain

$$\begin{bmatrix} A_1 \\ B_1 \end{bmatrix} = \frac{1}{t_{12}} \begin{bmatrix} 1 & r_{12} \\ r_{12} & 1 \end{bmatrix} \begin{bmatrix} A_2 \\ B_2 \end{bmatrix} = D_{12} \begin{bmatrix} A_2 \\ B_2 \end{bmatrix} \quad (4.15)$$

Where r_{12} , t_{12} are the Fresnel reflection and transmission coefficients, D_{12} is

defined as the transition matrix between dielectric layer 1 and 2. It is depend on the polarization of light, thus problem is often treated separated for different polarization state.

After realized the transition matrix relates the fields on both sides of medium interface, now we need to consider a propagation matrix to solve the wave propagating in a homogenous layer with refractive index (n) and thickness (d), as shown in Fig. 4-6

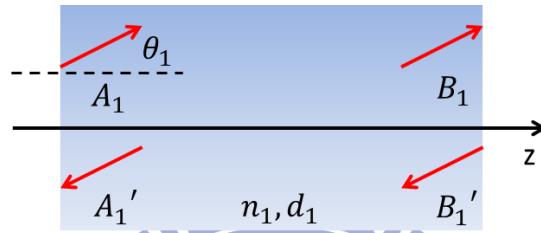


Fig. 4-6 Geometry for propagation matrix.

$$\begin{bmatrix} A_1 \\ B_1 \end{bmatrix} = \begin{bmatrix} e^{-i\varphi_1} & 0 \\ 0 & e^{i\varphi_1} \end{bmatrix} \begin{bmatrix} A_1' \\ B_1' \end{bmatrix} = P_1 \begin{bmatrix} A_1' \\ B_1' \end{bmatrix}, \varphi_1 = k_0 \times n_1 \times d_1 \times \cos\theta_1 \quad (4.16)$$

Where P_1 is defined as the propagation matrix. For lossless media, propagation matrix is unitary. Combining the transition matrix and the propagation matrix, we can deal with the general multilayer structure very fast. Considering N-layer structures which is illustrated in Fig. 4-7, the amplitudes (A_0, B_0) in medium 0 is related to medium N (A_N, B_N) by following relationship.

$$\begin{aligned} \begin{bmatrix} A_0 \\ B_0 \end{bmatrix} &= D_{01} P_1 D_{12} P_2 \dots D_{N-2,N-1} P_{N-1} D_{N-1,N} \begin{bmatrix} A_N \\ B_N \end{bmatrix} \\ &= \begin{bmatrix} M_{11} & M_{12} \\ M_{21} & M_{22} \end{bmatrix} \begin{bmatrix} A_N \\ B_N \end{bmatrix} = M \begin{bmatrix} A_N \\ B_N \end{bmatrix} \end{aligned} \quad (4.17)$$

Where M is transfer matrix, once the matrix is obtained, the information of Fresnel coefficients of the multilayer structure can be calculated.

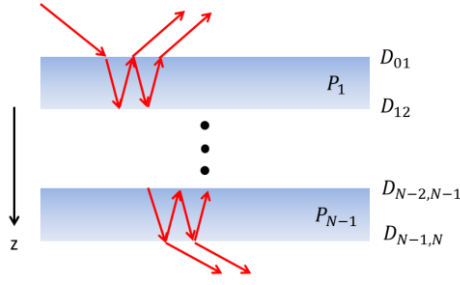


Fig. 4-7 Schematic drawing showing the matrix method.

Then, we set the beam is launched, therefore, $B_N = 0$, and According Eq. (4.17),

$$A_0 = M_{11}A_N \quad (4.18a)$$

$$B_0 = M_{12}A_N \quad (4.18b)$$

The Fresnel coefficients are given by

$$r = \frac{A_0}{A_N} = \frac{1}{M_{11}} \quad (4.19a)$$

$$t = \frac{B_0}{A_0} = \frac{M_{21}}{M_{11}} \quad (4.19a)$$

Following this method, the effect of MIM structure can be calculated.

4.4 Simulation and Experimental Data

Firstly, we show the effect of SVP passing through the linear polarizer and compare the excitation of SPR between simulation and experimental data. Secondary, the effect of MIM structure will be confirm by sensing the different refractive indices. Finally, we combined the radially polarized white light and MIM structure to detect the different concentration of salt solution.

Fig. 4-8 shows that donut-shaped intensity profile of radially polarized white light and the unique profiles which passes through different direction of transmitted axis of analyzer. The results of Fig. 4-8 demonstrate the preliminary effect of SVP, and then the effect will be further demonstrated by the excitation of SPR.

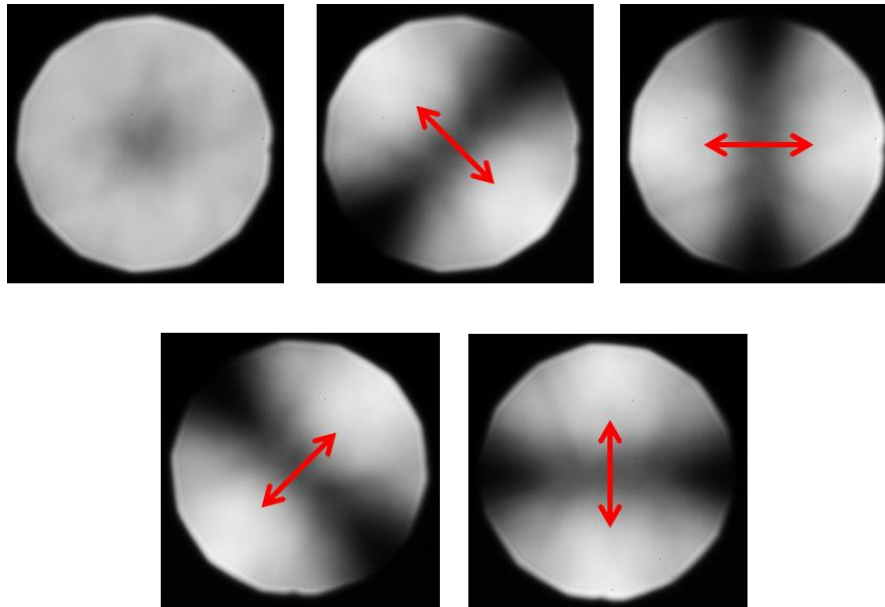


Fig. 4-8 Radially polarized white light generated by SVP. The arrows indicate the axis direction of analyzer.

To demonstrate the excitation of chromatic SPR, we choose three specific wavelengths to compare with simulated results; the chosen wavelength is 610 nm, 530 nm, and 450 nm, respectively. For simplifying the comparison, we do not consider the effect of MIM structure; it means that the structure is only a gold monolayer.

The comparison between Fig. 4-9 (a) and Fig. 4-9 (b) shows that the experimental results strongly agree with our simulation predictions. Therefore, the effect of SVP is demonstrated. In the past, that is impossible to simply achieve. In addition, for different operation purpose, the SVP device can be extended to create arbitrary stat of polarization without loss of generality.

The effect of MIM structure which can extend the sensing range will be verified by sensing in different refractive indices. Fig. 4-10 shows the reflective disk for different sensing condition and set the radius of disk is unity. By analyzing the distance between the central to SPR dip and the difference distance between different sensing condition, we can find the MIM structure acturely supports an additional SPR

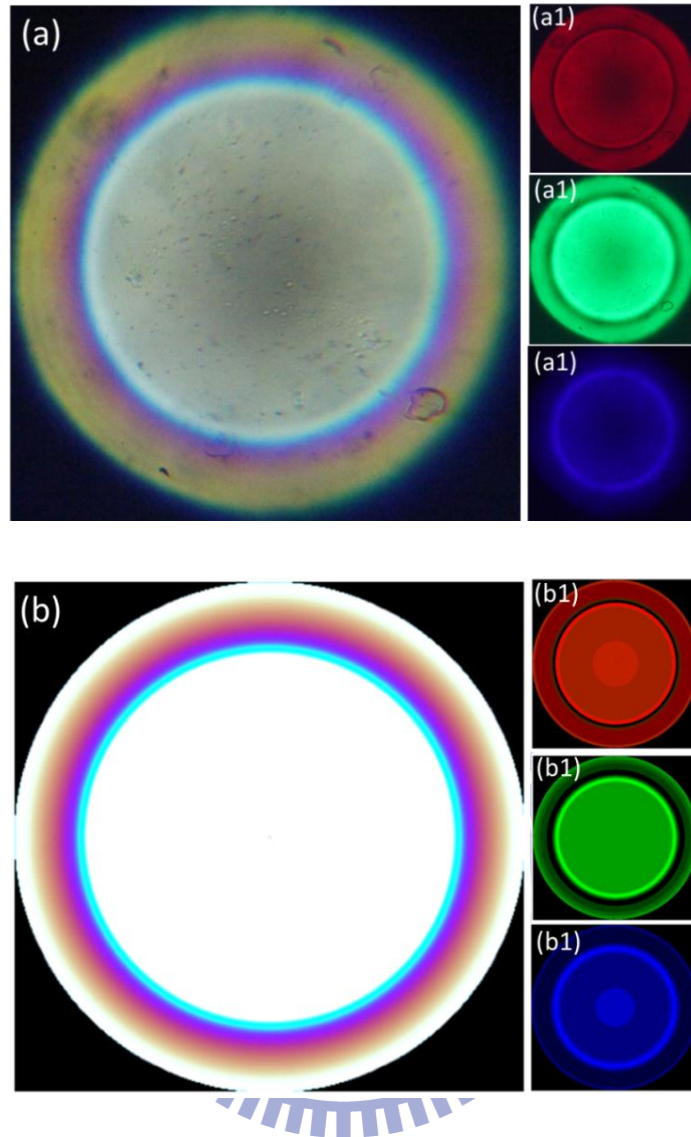


Fig. 4-9 The (a) experimental and (b) simulated observation of reflected rainbow disk for the case of free space in contact with the gold monolayer structure, where subfigures 1 to 3 are respectively show the dark resonance ring observed at wavelength $\lambda = 610$ nm, 530 nm, and 450 nm.

solution which can be excited by smaller propagating constant.

The MIM structure was proposed to overcome the barrier of detecting limitation of an objective based SPR sensor which is restricted by the NA of objective lens. The MIM structure provides provides additional 11% observation window. It

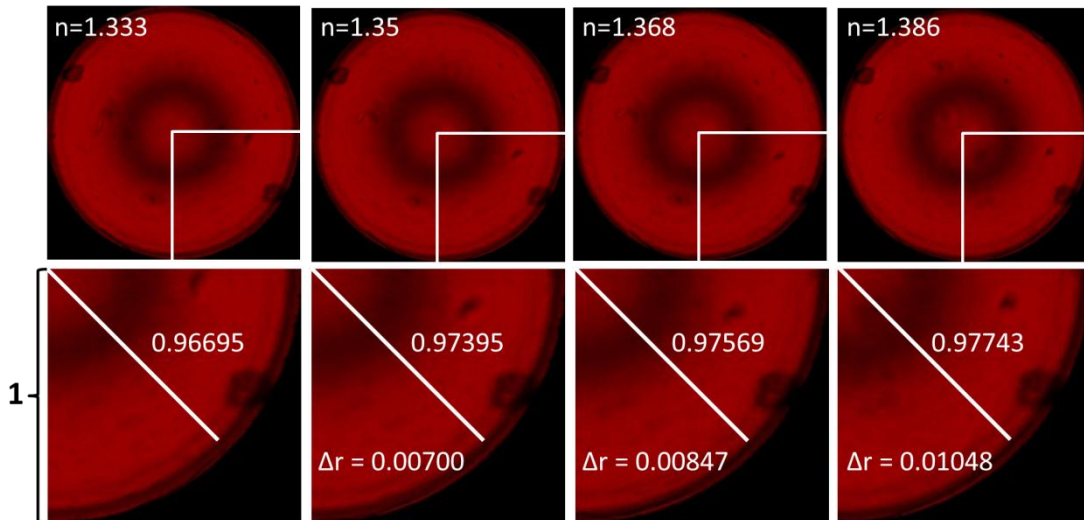


Fig. 4-10 Comparison shows the effect of MIM structure ($\lambda=610\text{nm}$).

increases sensing range up to 1.42 and covers the general usage in bio-molecular detection

Combining with radially polarized white light and MIM structure, we are not only able to analyze the diameter change of dark ring in a larger sensing range at individual wavelength by switching color filters, but also by integrating the area of reflective disc via spectrum analyzer to monitor the refractive index change of test sample. As the results, we proposed a scenario to analyze the NaCl solution with different concentration to validate the technique and proposed model. The sample was prepared by diluting a saturated salt solution. By integrating the intensity ratio of the concentric spectral component via an additional spectrometer (Chung-Yu, USB-100), a series of differential curves shown in dash lines feature two absorption peaks, which is due to the non-uniformity of lighting source, as shown in Fig. 4-11. In order to remove the weighting bias of illumination light at different wavelength, a normalized deviation between salt solution and the condition of pure water is also demonstrated, which indicates 466 nm, 566 nm, and 650 nm are relatively sensitive observation windows in visible for monitoring the concentration change of a salt solution.

Therefore, it provides a great feature of indicating suitable observation window for researchers to study individual bio-sample.

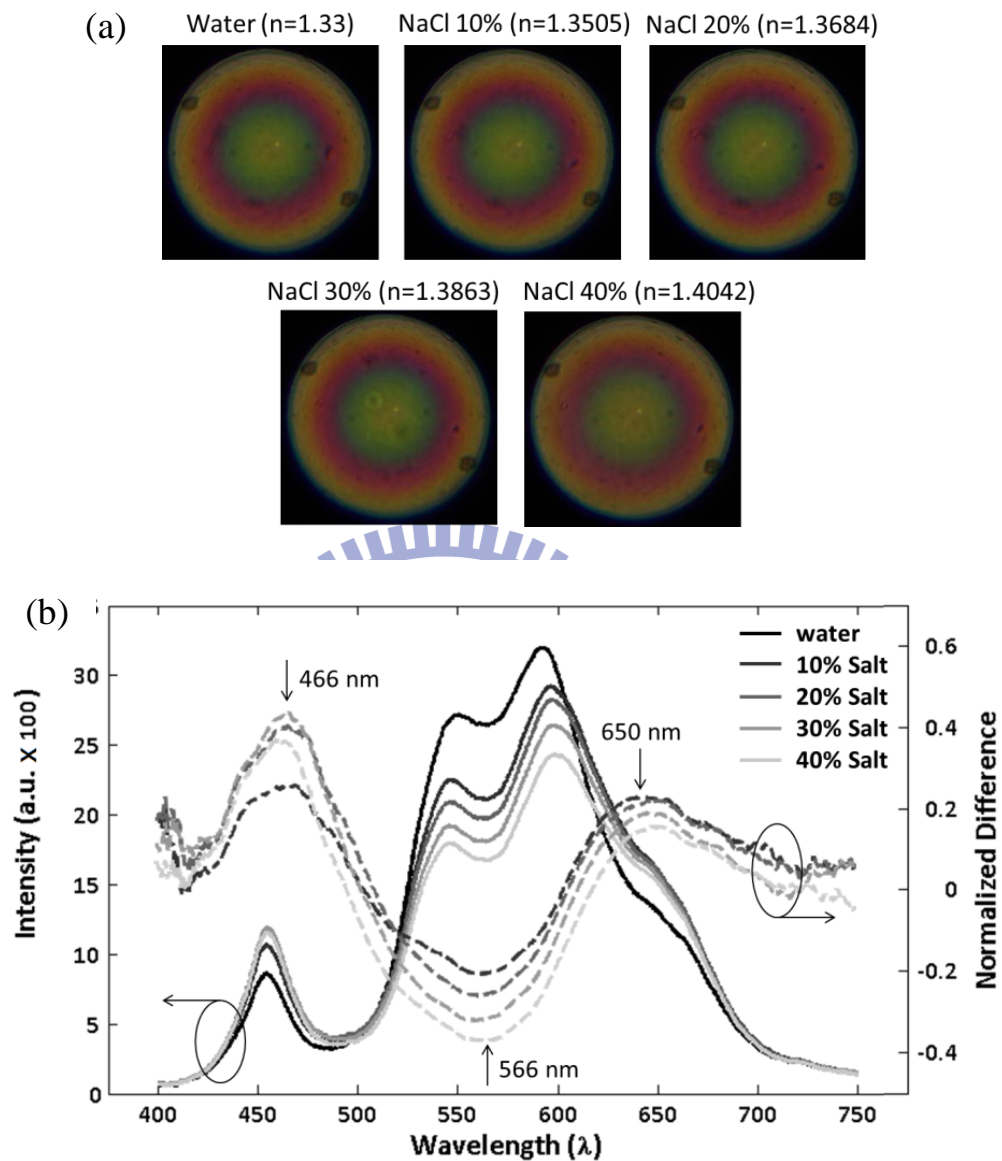


Fig. 4-11 (a) rainbow concentric ring in different sensing condition (b) the spectra distribution of rainbow concentric rings as the medium above the MIM structure is chosen saline with different concentration.

4.5 Summary

The advantages of PC-RPSPR sensor is not only to provide rich SPR information of a local region at one time, which reveals the resonance angle of SPR

for different wavelength, but also to supply larger sensing range. We demonstrated a unique pattern with rainbow concentric ring which is generated by a PC-RPSPR sensor integrated with a broadband radial polarizer and the practical influence of MIM light coupler. Based on this configuration, a full color SPR wave is able to excite and use to sense test samples with refractive index up to 1.42 covering most of living cells. The rainbow concentric ring is rich and save all of SPR information regarding to angular and wavelength spectra of a subwavelength-sized local region.



Chapter 5

Conclusions and Future work

5.1 Conclusions

In this thesis, we demonstrate two methods to extend the DoF, one is the synthesis method of two orthogonal inhomogeneous beams, and the other is the higher-order radial polarization method. The former takes advantages of the orthogonality between two orthogonal polarizations, the polarization coded aperture is equivalent to the adding of two apertures. The latter is based on high longitudinal component to top axial distribution in focal volume. Using these concepts and based on the simulation, different combinative ratio of two inhomogeneous polarizations and different order of radial polarization all influence the effect of extended DoF.

Secondly, we demonstrate the production of chromatic radial polarization coded aperture. For sensing application, the chromatic radial polarization can excited chromatic SPR, providing the resonance angle for different wavelength of a local region at one time. Therefore, we build up a PC-RPSPR sensor; through integrating the area of reflective disc via spectrum analyzer can supply another route to monitor the characteristic properties of test sample. Furthermore, in order to optimize the sensor, we also demonstrated that the purposed MIM structure can extend the refractive index sensing range up to 1.42 in a 1.45 NA objective lens, which covers the general usage in bio-molecular detection.

Finally, we proposed a scenario to analyze the NaCl solution with different concentration to validate the capability of PC-RPSPR sensor.

5.2 Future work

So far, we already confirm the effect of sensor system, the unique pattern with rainbow concentric ring involves the rich information in local region, which is similar to the size of a focused spot, in order to completely bring out the advantage of the PC-RPSPR sensor. Next step, the dimension of detection will be extend to two-dimensions from one-point by scanning operation, the obtained information can constitute to a data cube, the data cube can present specific images of each specific wavelength respectively. The specific images is more clearly and helpful to analyze the characteristic properties of test sample. By scanning operation, the final objective is that obtain a three-dimensional wavelength dependent refractive-index map of cell structure. As shown in Fig. 5-1.

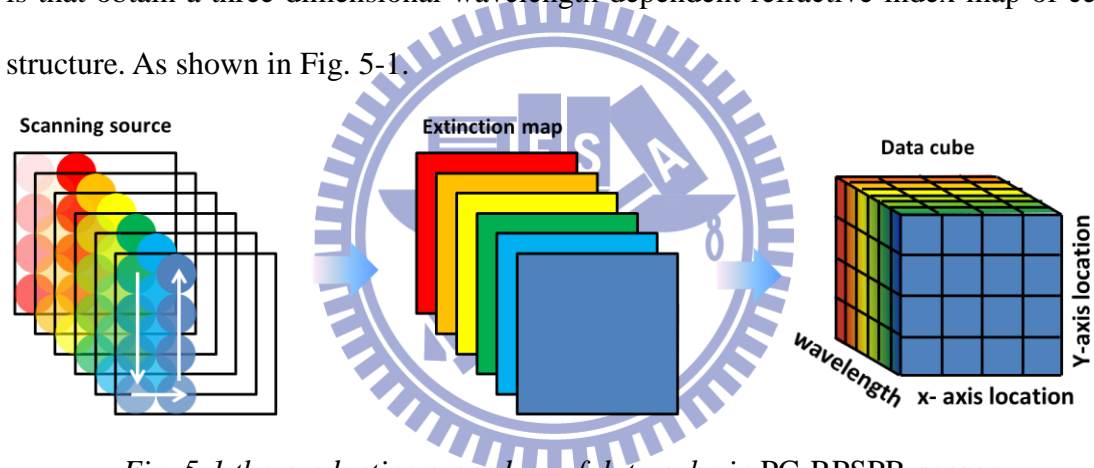


Fig. 5-1 the productive procedure of data cube in PC-RPSPR sensor

Moreover, the defocusing error may occur in the scanning procedure, therefore, the technique of extended DoF could be employed to decrease the influence of z-axis by combining the radial polarization and azimuthal polarization. In addition to use the extended DoF technique, the sensitivity of this sensor could be further enhanced by coating gold nanoparticles on the top of metal surface. Also, it can integrate with super continuum laser source to exploit surface-enhanced Raman scattering for more applications.

References

- [1] J. W. Goodman, *Introduction to Fourier Optics* (McGraw-Hill, New York, 1968).
- [2] W. Singer, M. Totzeck, H. Gross, *Handbook of Optical System 2: physical image formation* (Wiley-VCH, Weinheim, 2005).
- [3] T. H. Lan and C. H. Tien, "Study on Focusing Mechanism of Radial Polarization with Immersion Objective," *Jpn. J. Appl. Phys.* **47** 5806–5808 (2008).
- [4] S. C. Tidwell, G. H. Kim, and W. D. Kimura, "Efficient radially polarized laser beam generation with a double interferometer," *Appl. Opt.* **32**, 5222–5229 (1993).
- [5] S. Takeuchi, R. Sugihara, and K. Shimoda, "Electron acceleration by longitudinal electric field of a Gaussian laser beam," *J. Phys. Soc. Jpn.* **63**, 1186–1193 (1994).
- [6] Q. Zhan, "Trapping metallic Rayleigh particles with radial polarization," *Opt. Express* **12**, 3377–3382 (2004).
- [7] L. E. Helseth, "Roles of polarization, phase and amplitude in solid immersion lens systems," *Opt. Commun.* **191**, 161–172 (2001).
- [8] V. G. Niziev and A. V. Nesterov, "Influence of beam polarization on laser cutting efficiency," *J. Phys. D* **32**, 1455–1461 (1999).
- [9] X. Hao, C. Kuang, T. Wang, and X. Liu, "Phase encoding for sharper focus of the azimuthally polarized beam," *Opt. Letters* **35**, 3928–3930 (2010)
- [10] E. H. Linfoot and E. Wolf, "Diffraction images in systems with an annular aperture," *Proc. Phys. Soc. B* **66**, 145–149 (1953).
- [11] W. T. Welford, "Use of annular apertures to increase focal depth," *J. Opt. Soc. Am.* **50**, 749–753 (1960).
- [12] J. H. Mcleod, "The axicon: a new type of optical element," *J. Opt. Soc. Am.* **44**, 592–592 (1954).
- [13] J. W. Y. Lit and R. Tremblay, "Focal depth of a transmitting axicon," *J. Opt. Soc. Am.* **63**, 445–449 (1973).

- [14] E. R. Dowski and W. T. Cathey, "Extended depth of field through wave-front coding," *Appl. Opt.* **34**, 1859-1866 (1995).
- [15] Y. Takahashi and S. Komatsu, "Optimized free-form phase mask for extension of depth of field in wavefront-coded imaging," *Opt. Lett.* **33**, 1515-1517 (2008).
- [16] Q. Yang, L. Liu, and J. Sun, "Optimized phase pupil masks for extended depth of field," *Opt. Commun.* **272**, 56-66 (2007).
- [17] W. Chi, K. Chu, and N. George, "Polarization coded aperture," *Opt. Express* **14**, 6634-6642 (2006).
- [18] Y. Kozawa and S. Sato, "Sharper focal spot formed by higher-order radially polarized laser beams," *J. Opt. Soc. Am. A* **24**, 1793-1798 (2007).
- [19] X. L. Wang, J. Ding, W. J. Ni, C. S. Guo, and H. T. Wang, "Generation of arbitrary vector beams with a spatial light modulator and a common path interferometric arrangement," *Opt. Lett.* **32**, 3549-3551 (2007).
- [20] Y. Kozawa and S. Sato, "Generation of a radially polarized laser beam by use of a conical Brewster prism," *Opt. Lett.* **30**, 3063-3065 (2005).
- [21] K. Yonezawa, Y. Kozawa, and S. Sato, "Generation of a radially polarized laser beam by use of the birefringence of a *c*-cut Nd:YVO₄ crystal," *Opt. Lett.* **31**, 2151-2153 (2006).
- [22] R. W. Wood, "On a remarkable case of uneven distribution of light in a diffraction grating spectrum," *Proc. Phys. Soc. London* **18**, 269-275 (1902).
- [23] U. Fano, "The theory of anomalous diffraction gratings and quasi-stationary waves on metallic surfaces," *J. Opt. Soc. Am.* **31**, 213-222 (1941).
- [24] R. H. Ritchie, "Plasma losses by fast electrons in thin films," *Phys. Rev.* **106**, 874-881 (1957).
- [25] E. A. Stern and R. A. Ferrell, "Surface plasma oscillations of a degenerate electron gas," *Phys. Rev.* **120**, 130-136 (1960).
- [26] S. Quabis, R. Dorn, M. Eberler, O. Glöckl, and G. Leuchs, "Focusing light to a tighter spot," *Opt. Commun.* **179** 1-7 (2000).

- [27] R. Dorn, S. Quabis, and G. Leuchs, “Sharper focus for a radially polarized light beam,” *Phys. Rev. Lett.* **91**, 233901 (2003).
- [28] G. Machavariani, Y. Lumer, I. Moshe, A. Meir, and S. Jackel, “Efficient extracavity generation of radially and azimuthally polarized beams,” *Opt. Lett.* **32**, 1468–1470 (2007).
- [29] M. Stadler and M. Schadt, “Linearly polarized light with axial symmetry generated by liquid-crystal polarization converters,” *Opt. Lett.* **21**, 1948–1950 (1996).
- [30] N. Passily, R. S. Denis, K. Ait-Ameur, F. Treussart, R. Hierle, and J. F. Roch, “Simple interferometric technique for generation of a radially polarized light beam,” *J. Opt. Soc. Am. A* **22**, 984–991 (2005).
- [31] S. C. Tidwell, G. H. Kim, and W. D. Kimura, ” Efficient radially polarized laser beam generation with a double interferometer,” *Appl. Opt.* **32**, 5222–5229 (1993).
- [32] A. Shoham, R. Vander, and S. G. Lipson, “Production of radially and azimuthally polarized polychromatic beams,” *Opt. Lett.* **31**, 3405–3407 (2006).
- [33] T. Grosjean, M. Suarez, and A. Sabac, “Generation of polychromatic radially and azimuthally polarized beams,” *Appl. Phys. Lett.* **93**, 231106 (2008)

